



**NAVAL
POSTGRADUATE
SCHOOL**

MONTEREY, CALIFORNIA

THESIS

**TRANSPORT IMAGING IN THE ONE DIMENSIONAL
LIMIT**

by

Stephen D. Winchell

June 2006

Thesis Advisor:

Nancy Haegel

Second Reader:

Gamani Karunasiri

Approved for public release; distribution is unlimited

THIS PAGE INTENTIONALLY LEFT BLANK

REPORT DOCUMENTATION PAGE			Form Approved OMB No. 0704-0188	
Public reporting burden for this collection of information is estimated to average 1 hour per response, including the time for reviewing instruction, searching existing data sources, gathering and maintaining the data needed, and completing and reviewing the collection of information. Send comments regarding this burden estimate or any other aspect of this collection of information, including suggestions for reducing this burden, to Washington headquarters Services, Directorate for Information Operations and Reports, 1215 Jefferson Davis Highway, Suite 1204, Arlington, VA 22202-4302, and to the Office of Management and Budget, Paperwork Reduction Project (0704-0188) Washington DC 20503.				
1. AGENCY USE ONLY (Leave blank)		2. REPORT DATE June 2006	3. REPORT TYPE AND DATES COVERED Master's Thesis	
4. TITLE AND SUBTITLE Transport Imaging in the One Dimensional Limit			5. FUNDING NUMBERS	
6. AUTHOR(S) Stephen David Winchell				
7. PERFORMING ORGANIZATION NAME(S) AND ADDRESS(ES) Naval Postgraduate School Monterey, CA 93943-5000			8. PERFORMING ORGANIZATION REPORT NUMBER	
9. SPONSORING /MONITORING AGENCY NAME(S) AND ADDRESS(ES) National Science Foundation Research Foundation CC 4411			10. SPONSORING/MONITORING AGENCY REPORT NUMBER DNR 20033397	
11. SUPPLEMENTARY NOTES The views expressed in this thesis are those of the author and do not reflect the official policy or position of the Department of Defense or the U.S. Government.				
12a. DISTRIBUTION / AVAILABILITY STATEMENT Approved for public release; distribution is unlimited			12b. DISTRIBUTION CODE	
13. ABSTRACT (maximum 200 words) Transport imaging is a SEM-based technique used to directly image the motion and recombination of charge in luminescent semiconductors, allowing for the extraction of transport parameters critical to device operation. In this thesis, transport imaging for 1D structures was initiated with work on sample preparation, modeling and initial characterization. One dimensional structures are being integrated into forefront electronics due to their inherent advantages in size, packing density and power consumption. In this work the one dimensional equation for steady state minority carrier recombination distribution solved for the Gaussian source is derived and results from numerical simulations are presented. The diameter of the SEM beam is determined experimentally allowing for accurate simulation parameters. Intensity and drift measurements on four batches of top-down wire structure samples, fabricated on a AlGaAs/GaAs/AlGaAs double heterostructure using a FIB, are presented. Significant decreases in luminescence in FIB exposed regions are reported. Spatial luminescence from single bottom-up GaN and ZnO nanowires deposited by metal initiated metal-organic CVD on Au and SiO ₂ substrates is imaged. CL spectra for GaN and ZnO, with peak intensities at 3.27 and 3.29 eV, are characterized. Finally, several suggestions for further research are offered including transport imaging on contacted bottom-up nanowires and a potential application of transport imaging to FIB damage characterization.				
14. SUBJECT TERMS Nanowire, Minority Carrier, Transport Parameters, FIB Damage, GaN, ZnO, Transport Imaging			15. NUMBER OF PAGES 83	
			16. PRICE CODE	
17. SECURITY CLASSIFICATION OF REPORT Unclassified	18. SECURITY CLASSIFICATION OF THIS PAGE Unclassified	19. SECURITY CLASSIFICATION OF ABSTRACT Unclassified	20. LIMITATION OF ABSTRACT UL	

THIS PAGE INTENTIONALLY LEFT BLANK

Approved for public release; distribution is unlimited

TRANSPORT IMAGING IN THE ONE DIMENSIONAL LIMIT

Stephen D. Winchell
Ensign, United States Navy
B.S., United States Naval Academy, 2005

Submitted in partial fulfillment of the
requirements for the degree of

MASTER OF SCIENCE IN APPLIED PHYSICS

from the

**NAVAL POSTGRADUATE SCHOOL
June 2006**

Author: Stephen D. Winchell

Approved by: Nancy M. Haegel
Thesis Advisor

Gamani Karunasiri
Second Reader

James H. Luscombe
Chairman, Department of Physics

THIS PAGE INTENTIONALLY LEFT BLANK

ABSTRACT

Transport imaging is a SEM-based technique used to directly image the motion and recombination of charge in luminescent semiconductors, allowing for the extraction of transport parameters critical to device operation. In this thesis, transport imaging for 1D structures was initiated with work on sample preparation, modeling and initial characterization. One dimensional structures are being integrated into forefront electronics due to their inherent advantages in size, packing density and power consumption. In this work the one dimensional equation for steady state minority carrier recombination distribution solved for the Gaussian source is derived and results from numerical simulations are presented. The diameter of the SEM beam is determined experimentally allowing for accurate simulation parameters. Intensity and drift measurements on four batches of top-down wire structure samples, fabricated on a AlGaAs/GaAs/AlGaAs double heterostructure using a FIB, are presented. Significant decreases in luminescence in FIB exposed regions are reported. Spatial luminescence from single bottom-up GaN and ZnO nanowires deposited by metal initiated metal-organic CVD on Au and SiO₂ substrates is imaged. CL spectra for GaN and ZnO, with peak intensities at 3.27 and 3.29 eV, are characterized. Finally, several suggestions for further research are offered including transport imaging on contacted bottom-up nanowires and a potential application of transport imaging to FIB damage characterization.

THIS PAGE INTENTIONALLY LEFT BLANK

TABLE OF CONTENTS

I.	INTRODUCTION	1
A.	BACKGROUND	1
B.	MILITARY RELEVANCE	3
C.	THESIS OVERVIEW	5
II.	TRANSPORT IMAGING THEORY AND MODELLING	7
A.	INTRODUCTION	7
B.	MODEL PARAMETERS AND ASSUMPTIONS	7
1.	Gaussian Generation Region and Beam Size	7
2.	The Low Injection Limit	11
C.	1D STEADY STATE MODEL	13
1.	The Non-homogeneous Second Order Differential Equation	13
2.	General Solutions for a Point Source	15
3.	Solution for a Gaussian Generation Region	17
D.	MODELING RESULTS	18
1.	Introduction	18
2.	Non-Normalized Diffusion Modeling	19
3.	Normalized Drift Modeling	19
4.	Comparison of 1D and 2D Normalized Drift Modeling	20
III.	EXPERIMENTAL APPARATUS AND SAMPLES	23
A.	EXPERIMENTAL APPARATUS	23
1.	The SEM	23
2.	SEM Modes	24
3.	Data Extraction	26
B.	SAMPLE PROPERTIES AND FABRICATION	26
1.	Sample Heterostructure	26
2.	Focused Ion Beam (FIB) Lithography in Wire Structure Fabrication	27
3.	Chemical Vapor Deposition (CVD) in Nanowire Fabrication	28
C.	FIRST SAMPLE BATCH	29
1.	Batch Fabrication	29
2.	Batch Sample Dimensions and Details	30
3.	First Batch Damage Considerations	30
D.	SECOND SAMPLE BATCH	33
1.	Batch Fabrication	33
2.	Batch Sample Dimensions and Details	35
3.	Second Batch Damage Considerations	36
E.	THIRD SAMPLE BATCH	37
1.	Batch Fabrication Details	37
2.	Batch Sample Dimensions	38

F.	FOURTH SAMPLE BATCH	39
1.	Batch Fabrication	39
2.	Batch Sample Dimensions	39
IV.	EXPERIMENTAL RESULTS	41
A.	INTRODUCTION	41
B.	TOP-DOWN WIRE STRUCTURES	41
1.	First and Second Sample Batches	41
2.	Third Sample Batch	42
3.	Fourth Sample Batch	44
C.	BOTTOM-UP WIRE STRUCTURES	48
1.	SEM and CL Micrographs	48
2.	Cathodoluminescence Spectra	51
3.	CCD Imaging of Nanowires	52
V.	CONCLUSIONS AND SUGGESTIONS FOR FURTHER RESEARCH	55
A.	SUMMARY AND CONCLUSIONS	55
1.	Top-Down Wire Structures	55
2.	Bottom-Up Wire Structures	58
B.	SUGGESTIONS FOR FURTHER RESEARCH	59
1.	Advances in Bottom-Up Nanowire Structures	59
2.	Increased System Resolution for Transport Imaging	60
3.	Transport Imaging as a Measurement of FIB Damage	61
	APPENDIX A: DATA EXTRACTION PROGRAM	63
	LIST OF REFERENCES	65
	INITIAL DISTRIBUTION LIST	67

LIST OF FIGURES

Figure 1.	7500x SEM Micrograph of GaN nanowire on SiO ₂ Substrate.....	2
Figure 2.	Evolution of Threshold Current for Semiconductor Lasers (adapted from [1]).....	4
Figure 3.	20x SEM Micrograph of the MRS-3 Sample.....	8
Figure 4.	Probe Current Dependence of 30 keV SEM Beam Profile Over Sample Discontinuity.....	9
Figure 5.	1D Beamwidth Comparison, L _d =3.6 μm.....	10
Figure 6.	1D and 2D Intensity Comparison, Linear and Log Scales, L _d =3.6 μm, n=30.....	19
Figure 7.	1D Drift Intensity Comparison, Linear and Log Scales, L _d =3.6 μm, n=30.....	20
Figure 8.	2D Drift Intensity Comparison, Linear and Log Scales, L _d =3.6 μm, n=30.....	20
Figure 9.	1D and 2D Drift Intensity Comparisons, Linear and Log Scales, L _d = 3.6μm, n=30.....	21
Figure 10.	Schematic of SEM System.....	23
Figure 11.	30 keV, 1x10 ⁻¹⁰ A, 1 Second Spot on GaAs Heterostructure (154 μm x 125 μm).....	25
Figure 12.	The AlGaAs/GaAs/AlGaAs Heterostructure.....	27
Figure 13.	1000x SEM Micrograph of 923 nm Wire Structure...	30
Figure 14.	550x SEM Micrograph of First Batch Sample CL Points.....	31
Figure 15.	Spatial Variation of CL Spectra on First Batch..	32
Figure 16.	SEM and Corresponding CL Data for 40 μm Wire....	32
Figure 17.	FIB Etched Well Area and Epitaxial Layer CL Spectra.....	33
Figure 18.	Processing Diagram for Second Batch Samples....	34
Figure 19.	100x SEM Micrograph of Contacted Second Sample Batch.....	Error! Bookmark not defined.
Figure 20.	7500x SEM Micrographs of 1.7 μm and 14 μm Structures.....	36
Figure 21.	550x and 12000x SEM Micrographs of 746 nm Wire Damage.....	37
Figure 22.	100x SEM Micrograph of Third Batch Samples.....	38
Figure 23.	1000x SEM Micrograph of Fourth Batch Sample....	40
Figure 24.	Comparison of Average Second Batch Wire Structure Intensity.....	42
Figure 25.	2000x, 30 keV, 1x10 ⁻¹⁰ A, 5 Second SEM Picture Mode CCD Exposure.....	43
Figure 26.	Comparison of Average Fourth Batch Wire Structure Intensity.....	45

Figure 27.	30 keV, 1×10^{-10} A, 0.35 Second Spot on GaAs Heterostructure, 0 and 20V bias ($170 \mu\text{m} \times 160 \mu\text{m}$).....	46
Figure 28.	30 keV, 1×10^{-10} A, 0.35 Second Spot Linescans on GaAs Heterostructure, 0 and $\pm 0.01 \text{ V}/\mu\text{m}$ bias.....	46
Figure 29.	30 keV, 1×10^{-10} A, 20 Second Spot on $0.8 \mu\text{m}$ wire structure, 0 and 20V bias ($136 \mu\text{m} \times 117 \mu\text{m}$).....	47
Figure 30.	30 keV, 1×10^{-10} A, 20 Second Spot Linescans on $0.8 \mu\text{m}$ wire structure, 0 and $\pm 0.13 \text{ V}/\mu\text{m}$ bias....	47
Figure 31.	2000x and 4000x SEM Micrographs of ZnO Nanowires, 15 keV, 1×10^{-10} A.....	49
Figure 32.	2000x and 4000x SEM Micrographs of GaN Nanowires, 15 keV, 1×10^{-10} A.....	49
Figure 33.	2000x SEM (left) and CL (right) Micrographs of ZnO Nanowires, 15 keV, 1×10^{-10} A.....	50
Figure 34.	2000x SEM (left) and CL (right) Micrographs of GaN Nanowires, 15 keV, 1×10^{-10} A.....	50
Figure 35.	10000x SEM (left) and CL (right) Micrographs of GaN Nanowires, 15 keV, 1×10^{-10} A.....	51
Figure 36.	CL Spectra of ZnO Nanowires and SiO_2 substrate, 15 keV, 1×10^{-10} A.....	51
Figure 37.	CL Spectra of GaN Nanowires and SiO_2 substrate, 15 keV, 1×10^{-10} A.....	52
Figure 38.	2500x, 15 keV, 1×10^{-10} A, 120 Second Image of GaN Nanowires.....	53
Figure 39.	2000x, 30 keV, 1×10^{-10} A, 120 Second Image of ZnO Nanowires.....	54
Figure 40.	Comparison of Average Second and Fourth Batch Wire Structure Intensities.....	56
Figure 41.	0 and $0.13 \text{ V}/\mu\text{m}$ bias $L_d=0.44 \mu\text{m}$, $n=30$ Simulation (left) and 30 keV, 1×10^{-10} A, 20 Second Spot Linescan.....	57

LIST OF TABLES

Table 1.	30 keV SEM Beamwidth Dependence on Probe Current.....	9
Table 2.	First Batch Sample Dimensions.....	30
Table 3.	Second Batch Sample Dimensions	Error! Bookmark not defined.
Table 4.	Third Batch Sample Dimensions.....	38
Table 5.	Fourth Batch Sample Dimensions.....	40
Table 6.	Third Batch Contacted Sample Resistance.....	43
Table 7.	Average Maximum 0.25 Second Spot Intensities, 30 keV, 1×10^{-10} A.....	44
Table 8.	Average Maximum 1 Second Spot Intensities, 30 keV, 1×10^{-10} A.....	44

THIS PAGE INTENTIONALLY LEFT BLANK

ACKNOWLEDGMENTS

I would like to thank Prof. Haegel for her brilliant ideas and guidance throughout every stage of the research and writing of this thesis. You have taught me a great deal about semiconductor physics and being a scientist. I am greatly indebted to you.

The research in this project builds on the work of Capt. David Luber, USMC and LCDR Mitch Bradley, USN and relied on Kirsten Alberi's expertise for FIB work at the Center for Electron Microscopy at Lawrence Berkeley National Laboratory. Mike Talmadge and Prof. Matt Coleman at Fairfield University supported the modeling work. Dr. Tom Boone from Hitachi Global Storage provided the GaAs double heterostructure and Dr. Woong Kim and Dr. Peidong Yang at the Molecular Foundry at Lawrence Berkeley National Laboratory provided the GaN and ZnO nanowire samples. Funding for this project came from National Science Foundation grant DMR 2003397.

Finally, I would like to thank my friends and family for the love and support they have shown me in this and every other part of my life.

THIS PAGE INTENTIONALLY LEFT BLANK

I. INTRODUCTION

A. BACKGROUND

The transport of free charge in semiconductor structures is fundamental to the operation of many modern optoelectronic and semiconductor devices. Photodiodes including solar cells, photomultipliers used in night vision systems and spontaneous and stimulated emission in Light Emitting Diodes (LEDs) and lasers are just a few of devices and physical processes in which free charge transport parameters such as carrier mobility are of critical importance.

Since the early 1970's much research in optoelectronic and semiconductor devices has been focused on decreasing device sizes due to both practical advantages, including increased packing densities and reductions in device production costs and power consumption, as well as physical advantages such as dimensional differences in the density of states (DOS)[1]. Quantum wells, fundamentally two dimensional (2D) structures, have found myriad applications in the fabrication of laser diodes, infrared (IR) quantum cascade lasers and High Electron Mobility Transistors (HEMTs) to name just a few [2]. Research in the field of one dimensional (1D) structures, referred to as nanowires, has already yielded many advances including nanowire field effect transistors (FETs), crossed nanowire p-n junctions, InP nanowire LEDs and even ultraviolet (UV) lasers made of single GaN nanowires much like the one pictured in Figure 1 [3,4,5]. Accurate measurement of transport parameters is an

important part of nanowire applications for all the above mentioned nanowire devices.

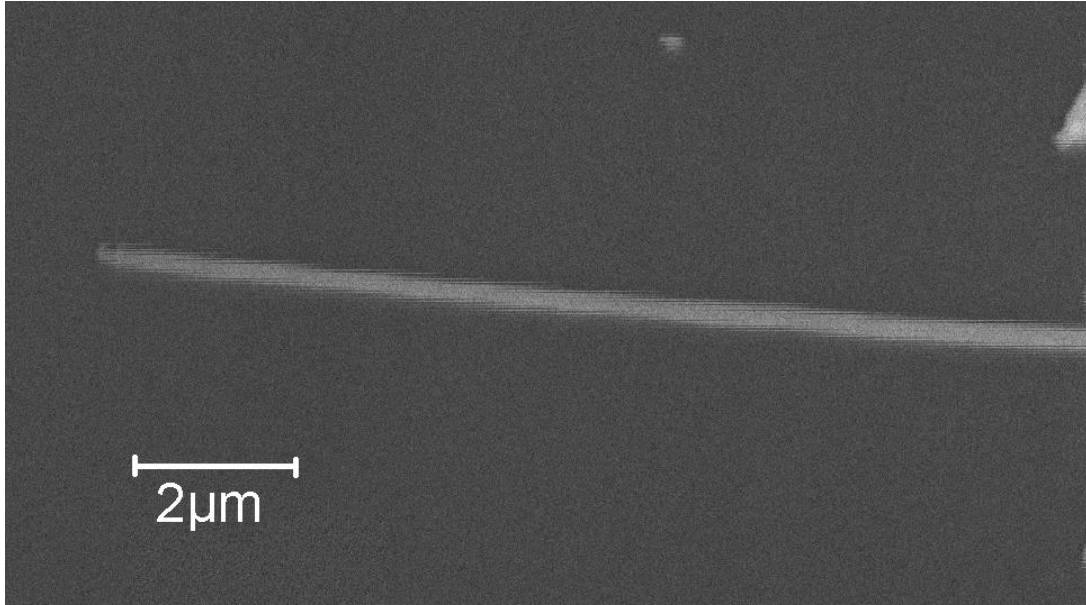


Figure 1. 7500x SEM Micrograph of GaN nanowire on SiO₂ Substrate

Traditional measurement of transport parameters in materials is done electrically, as in diffusion length measurements performed through electron beam induced current (EBIC) experiments. Electrical measurements are often affected by contact related phenomena that require potentially expensive and damaging sample processing. In view of this, a contact free technique called 'transport imaging' was developed in our laboratory in 2004 [6].

Transport imaging employs an optical microscope (OM), internal to a scanning electron microscope (SEM), in order to directly image the spatial recombination of charge generated by electron irradiation at a point. Planar contacts can be used to create local fields so that both diffusive and drift behavior can be directly observed. This has been successfully performed in two dimensional

heterostructures [6,7] and in bulk materials. One goal of this thesis is to advance the technique by investigating its initial applications to 1D structures.

The SEM-based approach also provides the benefit of high resolution for excitation and an ability to easily excite wide bandgap materials. The transport imaging method makes it possible to extract key materials parameters, such as diffusion lengths and minority carrier mobility, from a single charge coupled device (CCD) picture.

B. MILITARY RELEVANCE

Solar cells and integrated circuits (ICs) on intelligence and communication satellites and laser target designators and night vision goggles (NVGs) in the battlefield are just a few of the roles optoelectronic and semiconductor devices play in the modern military. Their importance cannot be overstated, and neither can the importance of the development of physical understanding and processes to advance these technologies.

One of the next steps in many of these technologies is the fabrication of nanowire based devices. A single nanowire, for example, can function as a stand alone cavity and gain medium, acting as a very narrow linewidth emission laser which could have many applications, including optical computing and microanalysis [4]. Reduced lasing threshold currents (see Figure 2) and diminished temperature dependence of the threshold current observed in nanowire lasers mean more efficient and compact uncooled laser devices [5]. Higher modulation factors in electro-optical modulators and new nanowire FETs may allow for faster, more

compact, efficient and inexpensive optical integrated circuits (OICs) and ICs [2]. As a result, DARPA and other agencies that support research and development for military optoelectronics are investing significant resources in nanotechnology.

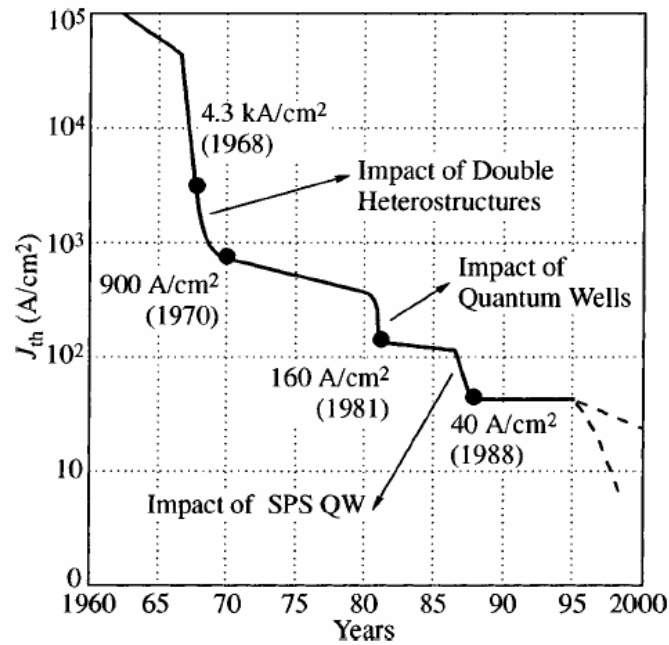


Figure 2. Evolution of Threshold Current for Semiconductor Lasers (adapted from [2])

Figure 2 shows the impact of the double heterostructure on threshold currents for semiconductor lasers. The result of the movement from 3D bulk materials to 2D double heterostructures allowed for reduction in threshold currents, lower power consumption and a reduction in physical dimensions that has put double heterostructure semiconductor lasers in every compact disk reader and many other optoelectronic devices. The military applications of nanowire technologies in semiconductor and optoelectronic devices could result in the same widespread revolution in technology.

C. THESIS OVERVIEW

In this work the transport imaging technique will be expanded to examine spatial luminescence from 1D structures in order to develop a contact free method of measuring carrier transport parameters. Transport is a key application of quantum wires. The possibility of direct measurement allows for more accurate transport parameter measurements and visualization of spatial variations along the length of the nanostructure. Effective application of the transport imaging method should allow the determination of values for minority carrier diffusion length and potentially, minority carrier mobility. These are important for devices, such as lasers, that depend on minority carrier injection. Transport characterization in quantum wires is still in a relatively early stage and the transport imaging technique would provide a unique way to extract important information.

Chapter II discusses the theoretical and experimental determination of the size of the SEM beam as well as the dynamics of electron beam-material interaction and carrier generation, critical to the SEM-based study of nanoscale structures. The one dimensional equation for steady state minority carrier recombination distribution solved for the Gaussian source is derived and results from numerical simulations based upon the previously developed equation are presented.

In Chapter III the experimental apparatus as well as the fabrication of multiple batches of wire structures on Beryllium (Be) modulation-doped p-type AlGaAs/GaAs/AlGaAs heterostructure using focused ion beam (FIB) lithography

are described. GaN and ZnO quantum wires grown by chemical vapor deposition (CVD) are also described in detail.

Chapter IV present the results of the luminous intensity and drift experiments carried out on the four separate batches of top-down wire structures and the cathodoluminescence (CL) spectra and results of different imaging techniques on the bottom-up nanowires. The final chapter provides an analysis of the previously obtained results and presents conclusions for both the top-down and bottom-up wire structures as well as ideas for future research.

II. TRANSPORT IMAGING THEORY AND MODELLING

A. INTRODUCTION

Transport imaging utilizes the combination of a SEM for high resolution charge generation and a Silicon CCD in conjunction with an OM for the recording of spatially resolved luminescence. Upon exposure to the electron beam, a steady state spatial distribution of luminescence associated with charge recombination is created which can then be recorded by the CCD. The CCD images can be analyzed in order to provide quantitative measurements of local minority carrier diffusion and drift lengths.

In order to extract minority carrier transport parameters from CCD images, the electron beam-material interaction and the subsequent generation, drift, diffusion and radiative recombination of carriers in the material must be modeled. The SEM beam's effects on the sample can be modeled as an extended generation region within the optically active GaAs layer of the sample. By employing certain simplifying assumptions, a model can be developed from the continuity equation which directly relates the spatial luminescence associated with minority carrier recombination to the minority carrier's diffusion and drift.

B. MODEL PARAMETERS AND ASSUMPTIONS

1. Gaussian Generation Region and Beam Size

It has been established experimentally that the SEM beam's intensity follows a Gaussian distribution to first

order. Theoretical calculations of the beam size assume that the beam diameter, defined as the Full Width at Half Maximum (FWHM) of the spot distribution, is the quadrature sum of the Gaussian probe electron beam and the various aberrations and has a beam diameter of ≈ 50 nm at 30 keV and 1×10^{-10} Amperes (A)[8].

In order to model the generation region, the goal was to experimentally determine the beam diameter of our SEM, because of potential deviation from theoretical or published values during operating conditions. A Geller Microanalytical Laboratories Magnification Reference Standard (MRS-3), pictured in Figure 3 below, was used to provide a high contrast, high resolution pattern.

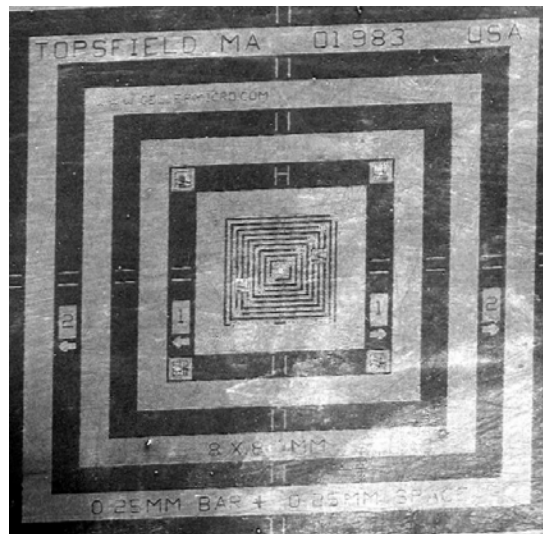


Figure 3. 20x SEM Micrograph of the MRS-3 Sample

Using the MRS-3, the rate of change of intensity along sharp edges of the control sample was correlated to the diameter of the SEM beam experimentally. The SEM beam profile over a discontinuity was measured under a constant

accelerating voltage of 30 keV at different probe currents, as shown in Figure 4.

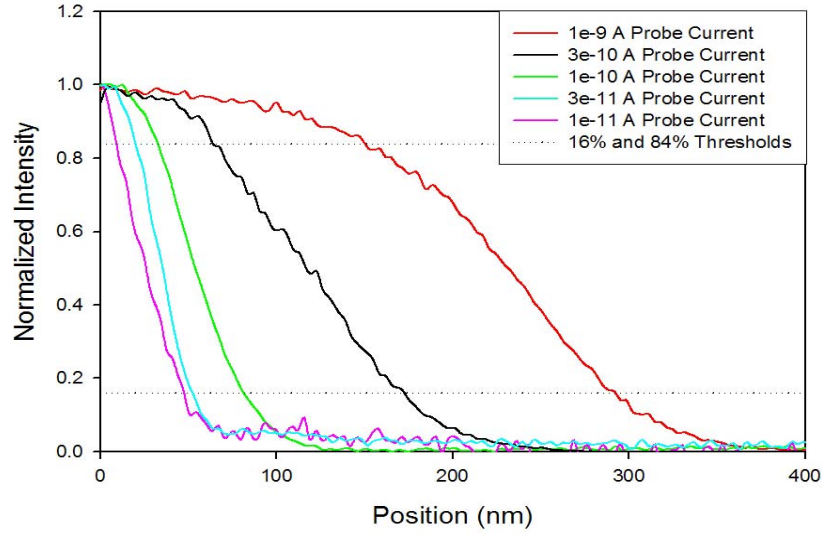


Figure 4. Probe Current Dependence of 30 keV SEM Beam Profile Over Sample Discontinuity

The beam intensity profiles obtained experimentally were analyzed and an empirical value for the SEM's beam width was calculated as a function of probe current. Values for 2σ , where σ is the standard deviation of the Gaussian distribution, were obtained from the positions of the 16% and 84% thresholds for beam intensity and converted into beamwidths following $FWHM = 2\sqrt{2\ln(2)}\sigma \approx 2.35\sigma$ [9].

Probe Current (A)	16%-84% (2σ) (nm)	FWHM (nm)
1×10^{-11}	34	40
3×10^{-11}	39	46
1×10^{-10}	48	56
3×10^{-10}	107	126
1×10^{-9}	139	163

Table 1. 30 keV SEM Beamwidth Dependence on Probe Current

The expected behavior as a function of probe current was observed as increasing the probe current increased the beam diameter and decreased the spatial resolution of the SEM. The SEM beam was measured to be a well focused beam (FWHM ≈ 50 nm) at low probe currents. A similar range of experiments could be carried out varying the accelerating voltage for a given probe current.

Modeling of the beam size's relation to the shape of the luminescent distribution shows a relative degree of insensitivity, especially when the beam FWHM $\ll L_d$, the diffusion length. This is even the case in the 1D diffusion scheme, which characteristically shows increased sensitivity to generation region variations. Figure 5 shows a comparison between 1D generation regions of 28 nm ($n=10$) and 166 nm ($n=60$), for an L_d of $3.6 \mu\text{m}$.

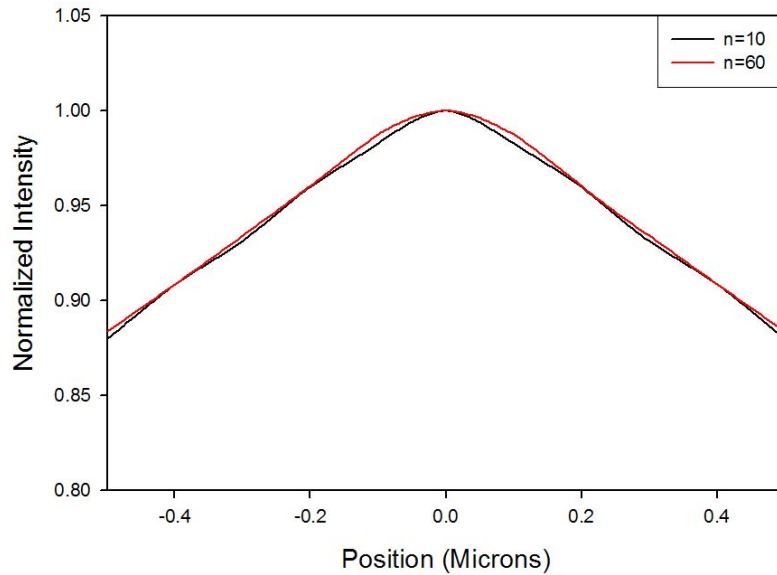


Figure 5. 1D Beamwidth Comparison, $L_d=3.6 \mu\text{m}$

The Gaussian distribution function $f(x) = \frac{n}{\sqrt{\pi}} e^{-n^2 x^2}$, where $n^2 = \frac{1}{2\sigma^2}$ can then be used to model the generation region of the electron beam from the SEM, where the value for $n \approx 30$ corresponds to a 30 keV, 1×10^{-10} A electron beam of width 56 nm. To first order, in the heterostructure material of interest, the generation region created by the incident SEM beam is approximated by the incident beam diameter on the surface, since the width of the layer is only ≈ 1000 Å.

2. The Low Injection Limit

In order for the spatial luminescence information recorded by the CCD to be a direct indication of the minority carrier distribution without resorting to more complex models, the minority carriers must be recombining into a much larger and effectively constant number of majority carriers. This is known as the low injection limit.

The number of holes and electrons per unit volume, p and n , can be calculated in the optically active GaAs region of the heterostructure to be $\approx 10^{18} \text{cm}^{-3}$ and $\approx 10^6 \text{cm}^{-3}$ respectively, at room temperature. Δp and Δn would then be the number of holes and electrons per unit volume generated by the electron beam incident on the material. In order for the low injection limit assumption to hold for the modeling, $\Delta p \ll p$ while $\Delta n \gg n$.

The maximum electron-hole pair generation rate, neglecting electron beam energy loss due to backscattering, can be calculated by $G = E_b / E_i$, where E_b is the incident

beam energy and E_i is the ionization energy of an electron-hole pair in GaAs. For electron beam energies in the 5-35 keV working range of the SEM, E_i is independent of incident electron beam energy and has been empirically determined to be $2.8E_g$ [10], where E_g is the bandgap of GaAs, ≈ 1.42 eV at 300 K. The total minority population is then $\frac{I}{e}G\tau$ where I is the probe current and τ is the minority carrier lifetime in the GaAs heterostructure, ≈ 4 ns.

The minority carrier concentration in the generation region can then be calculated by using a hemispherical generation volume approximation for a 30 keV, 10 nA electron beam, following the development of Kanaya and Okayama [11]. This yields a minority carrier concentration of $\approx 10^{16} \text{cm}^{-3}$. This value is an overestimate of the minority carrier concentration due to surface recombination and the dimension of the sample ($0.175 \text{ }\mu\text{m}$) relative to that of the beam penetration ($2\text{-}5 \text{ }\mu\text{m}$) and is still over two orders of magnitude lower than the effective majority carrier population due to doping of the GaAs in the samples of interest. All experimental work will be done below the low injection limit of a 30 keV, 1 nA electron beam.

Within the low injection limits the model is valid, but some effects are not physically observable. In the case of very short diffusion lengths in materials such as GaN ($L \approx 0.1 \text{ }\mu\text{m}$) that approach the optical imaging system's resolution of $\approx 0.4 \text{ }\mu\text{m}$, the simulated effects cannot be observed. In very large diffusion length materials such as GaInAs solar cell heterostructures ($L \approx 130 \text{ }\mu\text{m}$) it is very difficult to stay within the low injection limits as the

carrier lifetimes can increase over three orders of magnitude, from ns to ms. In addition, recombination in these materials occurs over such a large area and can be below the required intensity per unit area to register above noise levels on the CCD.

C. 1D STEADY STATE MODEL

1. The Non-homogeneous Second Order Differential Equation

The top-down wire structures described in Chapter III vary from 1D ($x \gg L_d$ and $y, z < L_d$) quantum wires to 2D ($x, y \gg L_d$ and $z < L_d$) heterostructures in their physical dimensions. The development of steady state carrier recombination models for all the wire structures is required; however, the model for 2D structures has been developed previously [6,7]. A 1D steady state equation is now developed, starting with the continuity equation for electrons in a p-type material:

$$\frac{dn}{dt} = G_n - U_n + \frac{1}{q}(\nabla \cdot \vec{J}_n) \quad (1)$$

where the time rate of change of electrons per unit volume, $\frac{dn}{dt}$, is expressed in terms of G_n and U_n , the generation and recombination rates per unit volume, and the divergence of \vec{J}_n , the current density vector. In the low injection limit $U_n = \frac{\Delta n}{\tau_n}$ where Δn and τ_n are the number of minority carriers

per unit volume and their respective lifetime. The current density for minority carriers can be defined as:

$$\vec{J}_n = q\mu_n n \vec{E} + qD_n \vec{\nabla} n \quad (2)$$

where μ_n is the mobility of electrons in GaAs, \vec{E} is the applied electric field within the material and D_n is the diffusion coefficient for electrons. Substituting Equation (1) into Equation (2) we arrive at:

$$\frac{dn}{dt} = G_n - \frac{\Delta n}{\tau_n} + \frac{1}{q} [\vec{\nabla} \cdot (q\mu_n n \vec{E} + qD_n \vec{\nabla} n)] \quad (3)$$

To simplify this expression, D_n can be related to the diffusion Length, L , by $D_n = \frac{L^2}{\tau_n}$, $\Delta n \approx n$ since $n_o \ll 1$ and, by definition, for the steady state there is no time dependence, so $\frac{dn}{dt} = 0$. We also realize that any gradient or external electric field will only exist in one dimension, arbitrarily \vec{x} , such that $\vec{E} = qE\vec{x}$ and $\vec{\nabla}^2 n = \frac{d^2 n}{dx^2}$. Equation (3) can now be written as:

$$0 = G_n - \frac{n}{\tau_n} + \mu_n E \frac{dn}{dx} + \frac{L^2}{\tau_n} \frac{d^2 n}{dx^2} \quad (4)$$

Equation (4) can be further simplified by the substitution $S = \mu_n \tau_n E$, where S is the drift length, and rearranged into a non-homogeneous second order differential equation:

$$\frac{\partial^2 n}{\partial x^2} + \frac{S}{L^2} \left(\frac{\partial n}{\partial x} \right) - \frac{1}{L^2} n = -\frac{G_n \tau_n}{L^2} \quad (5)$$

2. General Solutions for a Point Source

The derivation of the one dimensional equation for steady state minority carrier recombination distribution is first solved for the point source, such that $G_n = \frac{gL}{\tau_n} \delta(x)$ where $\delta(x)$ is the delta functional. Equation (5) then becomes:

$$L^2 \frac{\partial^2 n}{\partial x^2} - S \left(\frac{\partial n}{\partial x} \right) - n = -gL \delta(x) \quad (6)$$

The Fourier transform can be taken of Equation (6) yielding:

$$-L^2 k^2 N(k) - ikSN(k) - N(k) = -gL \quad (7)$$

Where $N(k)$ is the Fourier transform of n . Equation (7) can be re-arranged to form:

$$N(k) = \frac{g}{L} \left(\frac{1}{k^2 + C_1 k + C_2} \right) \quad (8)$$

where the constants $C_1 = \frac{iS}{L^2}$ and $C_2 = \frac{1}{L^2}$. The operation of completing the square can then be performed on the denominator of the expression in Equation (8)

$$k^2 + C_1 k + C_2 = \left(k + \frac{C_1}{2} \right)^2 + C_3^2 \quad (9)$$

where $C_3 = \frac{\sqrt{S^2 + 4L^2}}{2L^2}$. After a change of variables $k' = k + \frac{C_1}{2}$ we arrive at:

$$N(k) = \frac{g}{L} \left(\frac{1}{(k')^2 + C_3^2} \right) \quad (10)$$

Equation (10) can then be multiplied by $\frac{C_3}{C_3}$ and inverse Fourier transformed:

$$n(x) = \frac{g}{LC_3} \int_{-\infty}^{\infty} e^{i\left(k' - \frac{C_1}{2}\right)x} \left[\frac{C_3}{(k')^2 + C_3^2} \right] dk' \quad (11)$$

Equation (11) can be recognized as a Fourier transform of an exponential in conjunction with a multiplicative exponential term, $e^{\frac{-C_1}{2}ix}$, yielding the one dimensional equation for steady state minority carrier recombination distribution solved for the point source:

$$n(x) = \frac{2gL}{\sqrt{S^2 + 4L^2}} e^{\frac{Sx}{2L^2}} e^{-\frac{\sqrt{S^2 + 4L^2}}{2L^2}|x|} \quad (12)$$

3. Solution for a Gaussian Generation Region

For the case of the source function, $G_n(x) = \frac{f(x)}{\tau}$, the solution to the point source can be generalized, as long as the function is a general member of a delta sequence, such that $\lim_{n \rightarrow \infty} \int_{-\infty}^{\infty} \delta_n(x) f(x) dx = f(0)$. The Gaussian distribution function

$$f(x) = \frac{n}{\sqrt{\pi}} e^{-n^2 x^2}, \quad \text{where } n^2 = \frac{1}{2\sigma^2}, \quad \text{satisfies these conditions.}$$

Following the development preceding Equation (10) a parallel equation can be derived which takes the modified source function into account:

$$N(k) = \frac{F(k)}{L^2} \left(\frac{1}{(k')^2 + C_3^2} \right) \quad (13)$$

where $F(k)$ is the Fourier transform of $f(x)$. The inverse Fourier transform of $N(k)$, $w(x)$, can be expressed as a convolution, that is $\mathcal{F}^{-1}(\mathcal{F}[f]\mathcal{F}[g]) \equiv f * g$:

$$w(x) = \frac{F(k)}{L^2} * \frac{1}{(k')^2 + C_3^2} \quad (14)$$

Applying the convolution theorem,

$$f * g \equiv \int_{-\infty}^{\infty} f(x') \left(\int_{-\infty}^{\infty} G(k) e^{ik(x-x')} dk \right) dx' \quad (15)$$

and taking advantage of the previously derived result in Equation (12) for the result of the Fourier transform of the second term, Equation (16) is obtained:

$$w(x) = \int_{-\infty}^{\infty} \frac{1}{L^2} \frac{n}{\sqrt{\pi}} e^{-n^2 x'^2} \left(\frac{2L^2}{\sqrt{S^2 + 4L^2}} e^{\frac{S(x-x')}{2L^2}} e^{-\frac{\sqrt{S^2 + 4L^2}}{2L^2} |x-x'|} \right) dx' \quad (16)$$

After rearranging, Equation (17) is final form of the one dimensional equation for steady state minority carrier recombination distribution solved for the Gaussian source:

$$w(x) = \frac{2n}{\sqrt{\pi} \sqrt{S^2 + 4L^2}} \int_{-\infty}^{\infty} e^{-n^2 x'^2} e^{\frac{S(x-x')}{2L^2}} e^{-\frac{\sqrt{S^2 + 4L^2}}{2L^2} |x-x'|} dx' \quad (17)$$

D. MODELING RESULTS

1. Introduction

The steady state carrier recombination models developed in the previous section can be used to calculate expected spatial intensity distributions. MATHCAD was used to calculate the single and double integrals numerically, employing a Romberg trapezoidal approximation with constraint and convergence tolerances of 0.001. Numerically the integration over an infinite generation region is not possible, so a finite integration over three standard deviations of the Gaussian generation region accounting for 99.7% of the total generation is used as an approximation.

2. Non-Normalized Diffusion Modeling

Non-normalized diffusion modeling of top-down wire structures shows a substantial expected difference in recombination intensity between the 1D quantum wires and 2D heterostructures, assuming relevant material parameters stay constant. At its peak, the expected intensity difference is approximately 30 times greater for a 1D drift scheme than a 2D drift scheme, as illustrated in Figure 6. On the logarithmic scale the slope of the 1D line is linear, while the function of the 2D line is a zeroth order modified Bessel function of the second kind whose slope is approximately linear far from the origin.

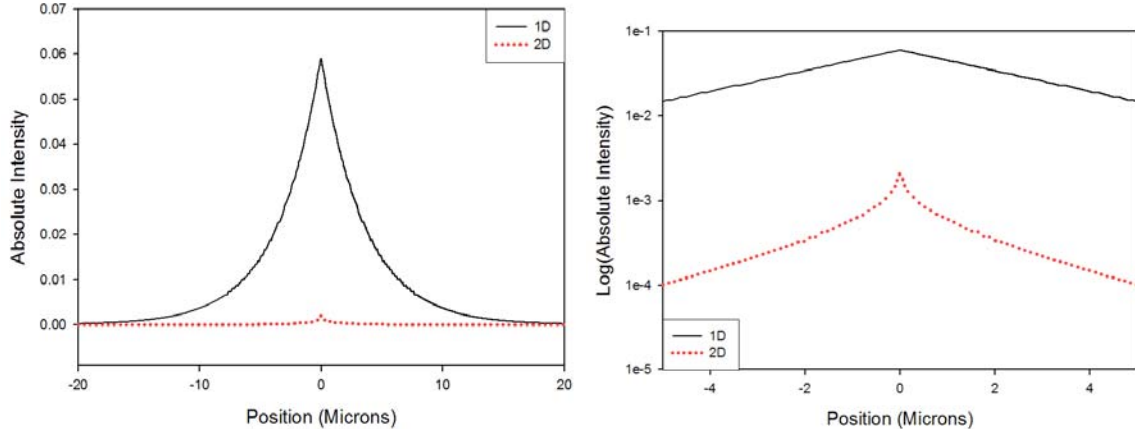


Figure 6. 1D and 2D Intensity Comparison, Linear and Log Scales, $L_d=3.6 \mu\text{m}$, $n=30$

3. Normalized Drift Modeling

While the non-normalized results demonstrate the clear difference between 1D and 2D intensities, normalization allows for a more effective comparison of the predicted shapes of spatial intensity distributions. This method of comparison is useful because of the absolute intensity fluctuations due to SEM optics and natural filament thermionic emission variations between experiments. Figures

7 and 8 show a change of three orders of magnitude in applied field on 1D and 2D structures and the resulting drift on both linear and logarithmic intensity scales:

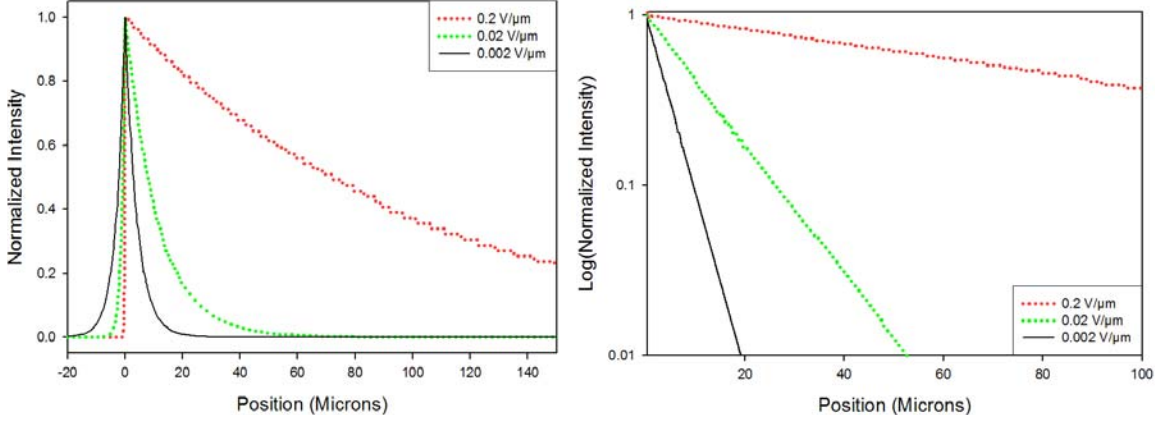


Figure 7. 1D Drift Intensity Comparison, Linear and Log Scales, $L_d=3.6 \mu\text{m}$, $n=30$

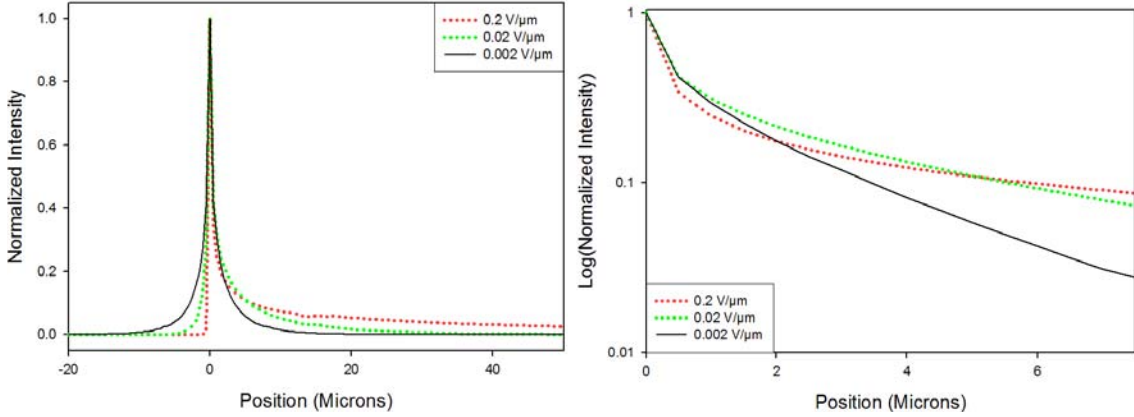


Figure 8. 2D Drift Intensity Comparison, Linear and Log Scales, $L_d=3.6 \mu\text{m}$, $n=30$

4. Comparison of 1D and 2D Normalized Drift Modeling

In the modeling process an arbitrary amount of electron-hole pairs are created in the generation region and their movement and recombination are simulated. By using the same generation regions and the same material parameters in the 1D and 2D models, only the dimensional

parameters affect the intensity and distribution of the luminescence.

In the 2D case, the generated charge drifts and diffuses into a region ($2\pi r dr$) which increases in direct proportional to the distance traveled. In the 1D case however, there is no change in the size of the region (dr) charge diffuses into with distance traveled. In practice, when the carrier diffusion lengths become much greater than the width of a sample heterostructure, an effectively 1D drift and diffusion scheme is created.

A comparison between 1D and 2D normalized drift characteristics shows differences in the shape of luminous intensity that increase with applied field. With increasing drift ($\mu_n \tau_n E$) lengths, proportional to increasing applied external fields, the effective confinement experienced by the minority carries increases. Due to this effect, transport in 1D is more sensitive to variations in material parameters. Figure 9 shows variation between 1D and 2D low and high applied field drift conditions on both linear and logarithmic scales:

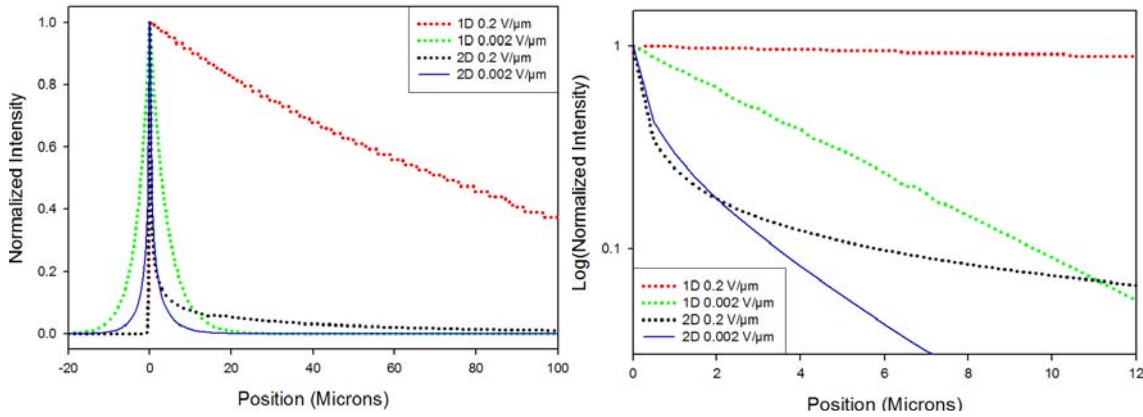


Figure 9. 1D and 2D Drift Intensity Comparisons, Linear and Log Scales, $L_d = 3.6\mu m$, $n=30$

THIS PAGE INTENTIONALLY LEFT BLANK

III. EXPERIMENTAL APPARATUS AND SAMPLES

A. EXPERIMENTAL APPARATUS

1. The SEM

A JEOL 840A SEM with an internal optical microscope (OM) and mirror assembly allowed for SEM, optical and CL imaging. An OM objective connected to a charge coupled device (CCD) camera or a mirror assembly connected to a CL system was inserted by means of retractable arms into the SEM chamber for data collection. The SEM system uses a constant flow liquid cooled stage which operates between room temperature and about 5K if liquid helium is used as the coolant. Figure 10 shows a schematic representation of the SEM system.

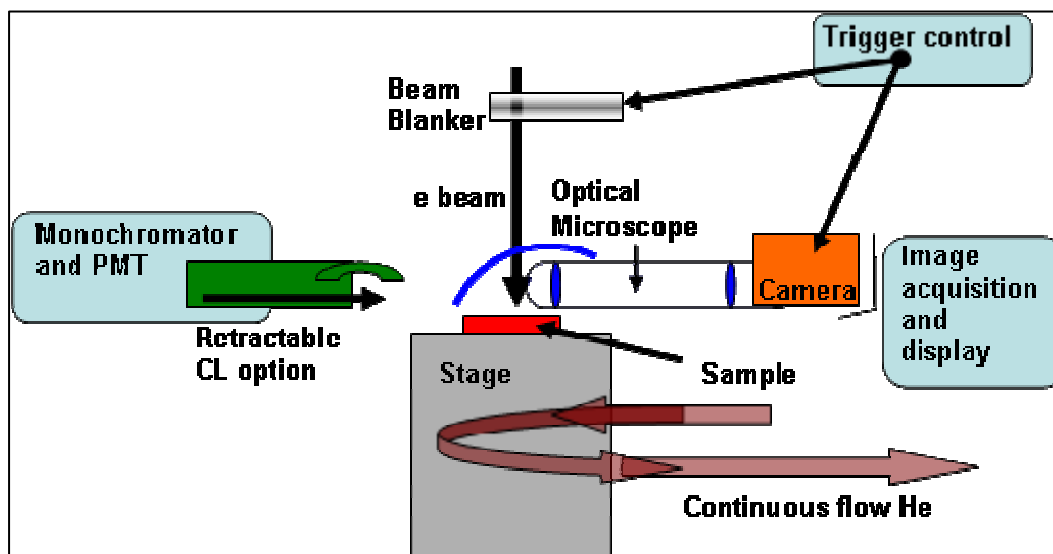


Figure 10. Schematic of SEM System

The Oxford Instruments CL system connected to the retractable mirror employs a parabolic mirror, $\frac{1}{4}$ m monochromator and TE cooled GaAs PMT as a detector. An

Apogee silicon CCD camera with a 2184x1472 pixel array serves as the optical detector connected to the retractable OM.

The Apogee CCD camera collects unfiltered light from about 300-1100 nm on a 15x10 mm CCD array. The CCD camera is thermoelectrically cooled to temperatures below -10°C to reduce noise during operation. Each pixel on the array has dimensions of 6.8 μm x 6.8 μm and the OM has a magnification of approximately 20x. This yields a CCD on sample resolution of about 0.4 $\mu\text{m}/\text{pixel}$. The resolution for incoherent light can be estimated as

$$\Delta y \approx \frac{0.61\lambda}{NA} \quad (18)$$

where Δy is the wavelength dependent spatial resolution, λ is the wavelength and NA is the numerical aperture. For the room temperature peak emission of GaAs (870 nm) and a numerical aperture of 0.95 (as a maximum value), Δy is found to be 0.56 μm . Thus the CCD resolution is close to the diffraction limit of 870 nm light characteristic of GaAs.

2. SEM Modes

The SEM can operate in picture, line and spot modes. Line and picture modes allow the beam to raster in a straight line or over a rectangular area, while spot mode focuses the beam down, as much as possible, to a point. SEM operating modes and magnifications can be chosen depending on the specific generation region shape and size desired.

In spot mode, the electron beam is focused down to a single point whose actual size depends primarily on probe current and accelerating voltage as discussed in Chapter II. Spot mode also displays a small secondary spot due to internal reflection in the OM optics, as seen in Figure 11.



Figure 11. 30 keV, 1×10^{-10} A, 1 Second Spot on GaAs Heterostructure ($154 \mu\text{m} \times 125 \mu\text{m}$)

Imaging with the SEM as well as sample measurements can be done in line and picture modes. Picture mode also serves as an ideal tool for fine focus adjustments in height for the optical system and can serve as a method for identifying important sample features relative to a spot when used in conjunction with spot mode operation during the same CCD exposure.

3. Data Extraction

Diffusion and drift spot data in the 1D limit takes on an exponential form, as described in Chapter II, which can be directly extracted from the value of the slope in the CCD pictures intensity profiles. Data from the line scan feature included in the Micro CCD software package or data from an imported image matrix in MATLAB can be used to obtain intensity profiles from CCD images. To reduce noise and locate and extract luminescence maxima from the TIF files in which CCD data is recorded a simple MATLAB program was used (see Appendix A).

B. SAMPLE PROPERTIES AND FABRICATION

1. Sample Heterostructure

All top-down samples were fabricated from a AlGaAs/GaAs/AlGaAs double heterostructure grown by solid source molecular beam epitaxy (MBE) on a semi-insulating substrate. Be was used to modulation dope the AlGaAs regions, making the optically active GaAs layer p-type. The minority carriers are electrons and within the GaAs layer there is an effective hole concentration of $\approx 1 \times 10^{18} \text{ cm}^{-3}$. Figure 12 illustrates the heterostructure dimensions.

Luminescence from the semi-insulating substrate is negligible compared to that of the epitaxial GaAs in CL measurements due its significantly lower level of optical activity relative to the GaAs.

$Al_{0.9}Ga_{0.1}As:Be$	250Å
$GaAs$	1000Å
$Al_{0.9}Ga_{0.1}As:Be$	500Å
Semi-insulating Substrate	

Figure 12. The AlGaAs/GaAs/AlGaAs Heterostructure

2. Focused Ion Beam (FIB) Lithography in Wire Structure Fabrication

In order to create the 'top-down' wire structures for carrier diffusion and recombination studies in this thesis, one of the methods used was FIB lithography. FIB is a technique in the semiconductor industry used in applications such as mask repair and site specific Transmission Electron Microscope (TEM) sample preparation. Exposing the heterostructure to the FIB served as a means of physically and electrically isolating the wire structure.

Inside the FIB system, a Ga liquid metal ion source (LMIS) is used to create ionized Ga ions which are then accelerated through a potential difference of 10-40 keV and focused with electrostatic lenses. When the high energy Ga ions strike the sample, the surface is amorphized and atoms on the surface are sputtered, which allows the sample

exposure to a FIB to be analogous to milling the exposed areas.

The FIB system also contains an SEM which operates at an offset of 52° from the FIB. The sample is connected to a stage which can be rotated to align it with the electron beam or the ion beam. Short of using the ion beam to image, however, the FIB etching must be done while viewed from a 52° offset which introduces challenges to milling exact structures.

3. Chemical Vapor Deposition (CVD) in Nanowire Fabrication

The 'bottom-up' nanowire structures studied in this thesis were deposited by metal initiated metal-organic CVD on Au and SiO₂ substrates. The process was carried out with different reagents in order to deposit both GaN and ZnO nanowires on the substrate at temperature of 800~1000 °C [14]. CVD is widely used in the semiconductor industry for thin film deposition.

In CVD the substrate is placed on a temperature controlled susceptor, made from a material resistant to the metalorganic compounds. Nitrogen gas is then bubbled through a metalorganic liquid and used as a carrier gas. In the case of GaN nanowires, nitrogen was bubbled through Trimethylgallium (TMG) to create a metalorganic vapor and introduced into the sample chamber with ammonia gas.

Thermally evaporated metals 2-10 nm thick on the substrate such as Ni, Fe and Au are then used as initiators for vapor-liquid-solid (VLS) nanowires. The VLS process begins with the dissolution of gaseous metalorganic

reactants into the liquid droplets of the catalyst metal. Nucleation and growth of singlecrystalline rods can then be achieved as the metalorganic vapors combine in on the seed crystal, allowing the growth of nanowires [14].

C. FIRST SAMPLE BATCH

1. Batch Fabrication

The fabrication of the first sample batch of top-down structures began with a methanol rinse of the fragment of the AlGaAs/GaAs/AlGaAs heterostructure to be etched by the FIB. In order to create an electric field within the sample for potential drift measurements, Platinum (Pt) pads for contacts were made on the sample by electron beam deposition.

In order to align the wire structures with the Pt pads, the sample was imaged by a 500 pA ion beam for a number of seconds before it was etched by the FIB, with 8-10 minute exposures to a 500 pA Ga ion beam. The electron beam deposition of Pt contacts and the subsequent imaging and etching by the FIB was repeated to fabricate all of the wire structures.

The sample was then rinsed in solution of Hydrochloric Acid (HCl) for 30 seconds to remove accumulated Ga on its surfaces produced by the FIB etching process.

2. Batch Sample Dimensions and Details

The first sample batch was fabricated with widths ranging from approximately 1 to 40 μm . High resolution SEM micrographs revealed variations in the wire widths of up to ± 100 nm, as illustrated in Figure 13. The irregularities in the attempted fabrication of uniform width structures also brings first sample batch fabrication methods into question. In Table 2 the error column is a combination of both measurement uncertainty and structure width variation.

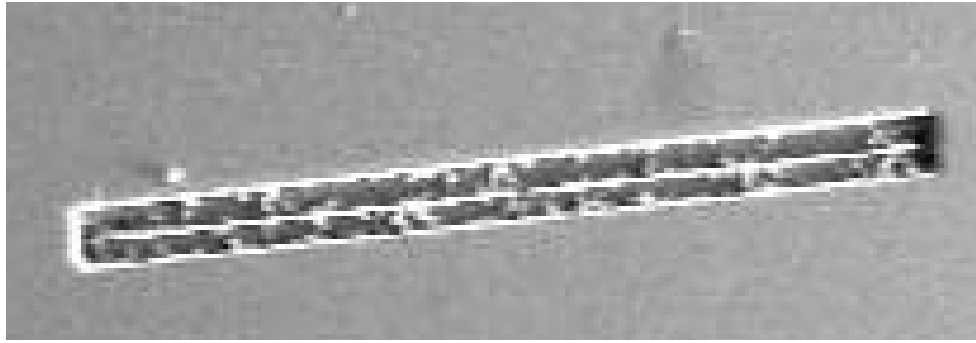


Figure 13. 1000x SEM Micrograph of 923 nm Wire Structure

Sample Number	Wire Width (nm)	Error (nm)	Error (%)
1	39150	± 100	0.26
2	9977	± 45	0.45
3	948	± 35	3.69
4	923	± 40	4.24

Table 2. First Batch Sample Dimensions

3. First Batch Damage Considerations

Measurements on and near the FIB etched wire structures displayed luminous intensities over 1000 times lower than measurements taken a few millimeters away and served as a clear indication of material damage associated

with decreased minority carrier lifetime in the vicinity of the wires. In order to understand and quantify the decrease in intensity in the vicinity of the wire structures, a series of CL spectra were taken. Figure 14 shows the four FIB etched wires, indicated by white arrows and the position of the CL spectra taken, indicated by the numbers 1 to 8. The spectra data points were evenly spaced in intervals of 465 μm .

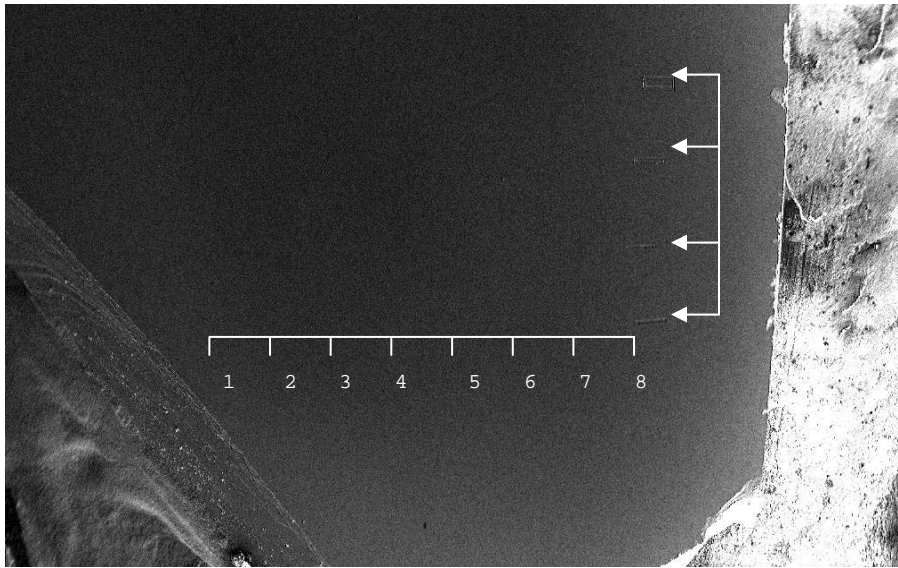


Figure 14. 550x SEM Micrograph of First Batch Sample CL Points.

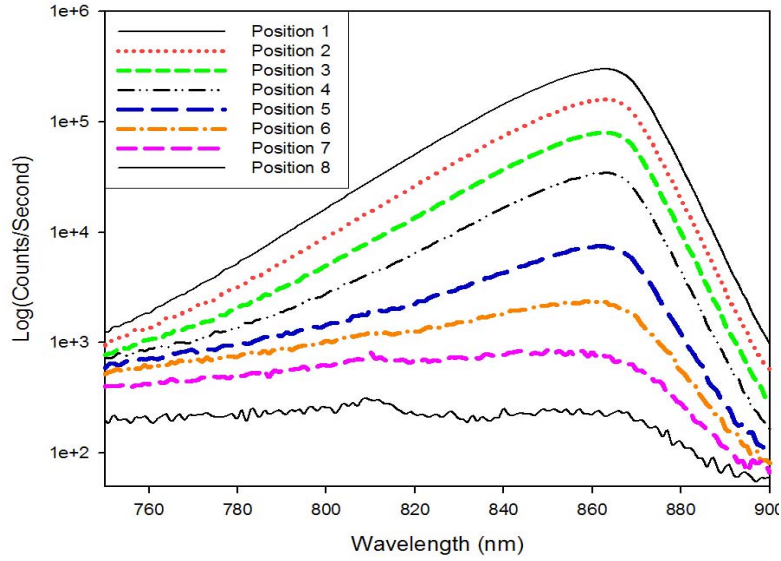


Figure 15. Spatial Variation of CL Spectra on First Batch

In the vicinity of the wire structures CL luminosity decreased significantly, and was only measurable in the areas where the substrate was exposed by the FIB process, as shown in Figure 16.

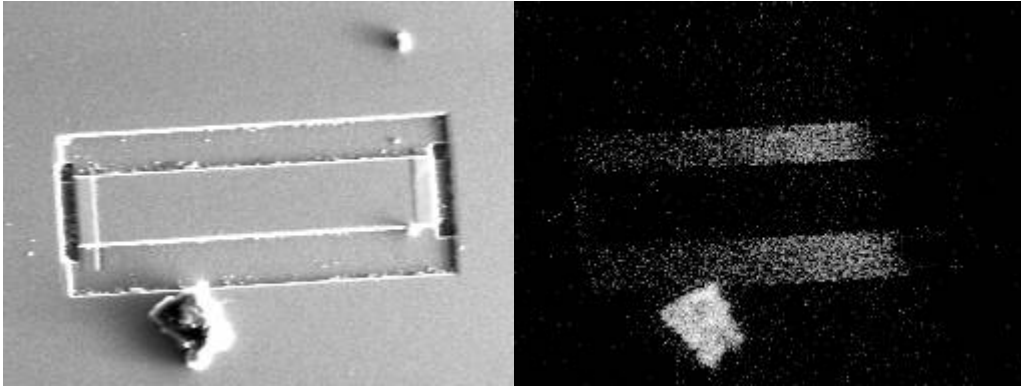


Figure 16. SEM and Corresponding CL Data for 40 μm Wire

Without the smaller bandgap heavily doped GaAs material covering the semi-insulating substrate in the FIB etched regions it was determined that observed luminosity came directly from the substrate rather than the epitaxial GaAs layer. Figure 17 shows broadening of the spectra and shift in energy peaks typical of heavily doped materials,

when comparing the doped GaAs and the FIB etched well substrate regions of the 40 μm wire structure.

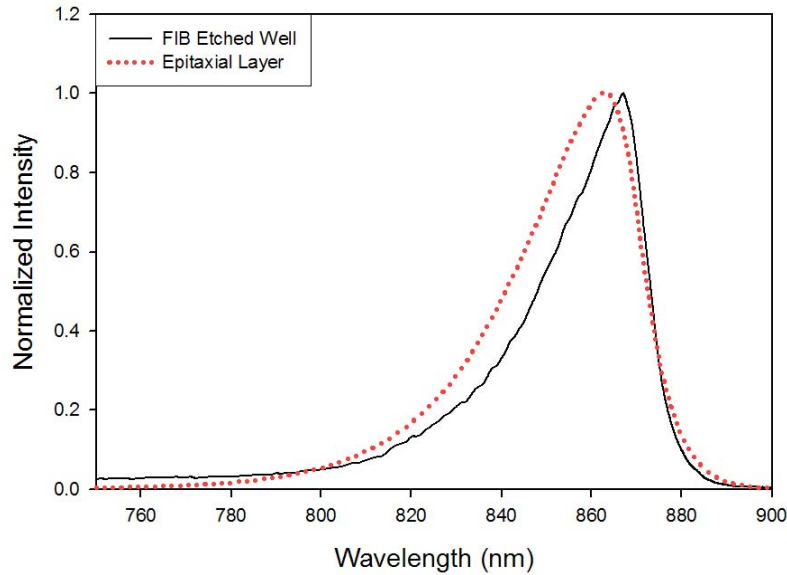


Figure 17. FIB Etched Well Area and Epitaxial Layer CL Spectra

The data collected on the first sample batch was clear evidence of large scale damage to the heterostructure material as well as large wire structure width variation. Exposure to the FIB imaging was enough to amorphize and etch surface of the material in the vicinity of the wire structures, altering its optical properties significantly, more than expected [15].

D. SECOND SAMPLE BATCH

1. Batch Fabrication

In order to reduce the damage to the sample that occurred in the fabrication of the first batch, isolating the wire structure region from FIB damage became a priority. In order to achieve this, contacting on the sample had to be done in a way that did not require FIB

imaging of the area. A 200 μm Silicon mask was affixed across the selected AlGaAs/GaAs/AlGaAs heterostructure fragment with wax to protect the area on which the wires would be etched from electron beam deposition of Ni/Ge/Au contacts that followed. Figure 18 gives a schematic representation of the area processing of the sample batch.

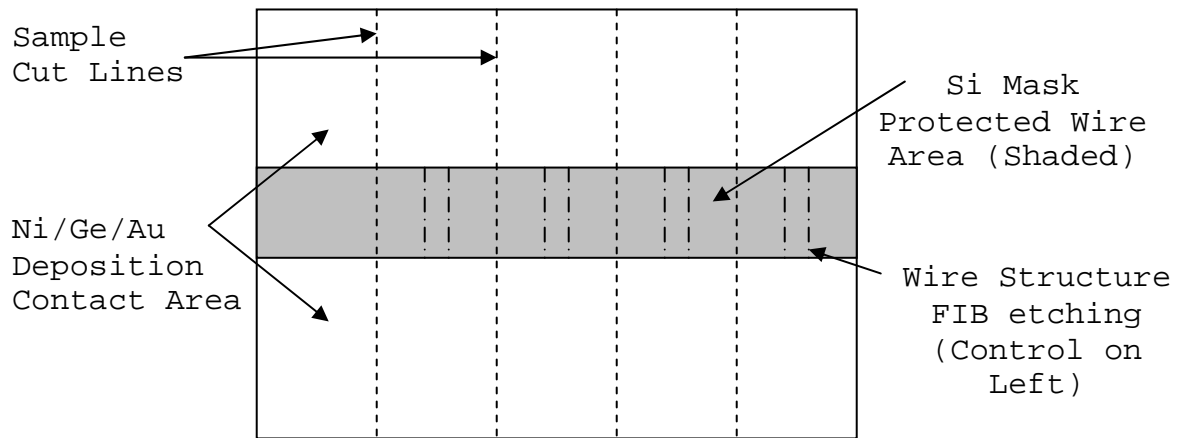


Figure 18. Processing Diagram for Second Batch Samples

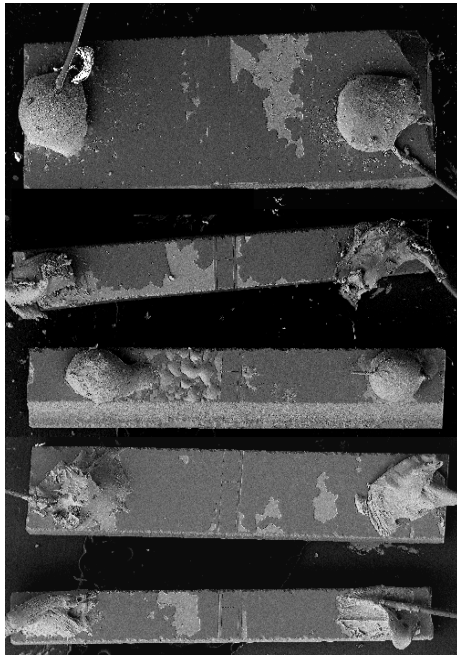
The silicon mask was then physically removed and methanol and xylene chemical rinses were used to clean the area. Rapid thermal annealing (RTA) of the contacts was then carried out at 430 $^{\circ}\text{C}$ for 20 seconds and the wire structures made in the non-metalized region of the sample using 8-10 minute 500 pA FIB etching. The sample batch was then sonicated in solution of HCl, causing the metal contacts to become detached from the sample.

The contact areas were then cleaned with low power oxygen plasma and the Si mask was reattached to the sample with wax. A second attempt at electron beam deposition of Ni/Ge/Au contacts also failed and after sonication in methanol and xylene chemical rinses the sample was cut with a wire saw, to electrically isolate each wire structure, as

show in Figure 18. Pressed In contacts were added to individual samples as required for application of external bias.

2. Batch Sample Dimensions and Details

The second sample batch was fabricated with wire structure widths which ranged from about 0.7 to 24 μm . No visual evidence of amorphization on the sample surface due to exposure to the FIB was present, but partially deposited contacts which failed to adhere to the sample surface are clearly visible in Figure 19.



Sample Number	Wire Width (nm)	Error (nm)	Error (%)
1	23630	± 85	0.36
2	13890	± 50	0.36
3	1725	± 20	1.16
4	746	± 35	4.69

Table 3. Second Batch Sample Dimensions
Figure 19. 100X SEM Micrograph of Contacted Second Sample Batch

A significant increase in the consistency of the wire widths was also observed, as shown in Figure 20.

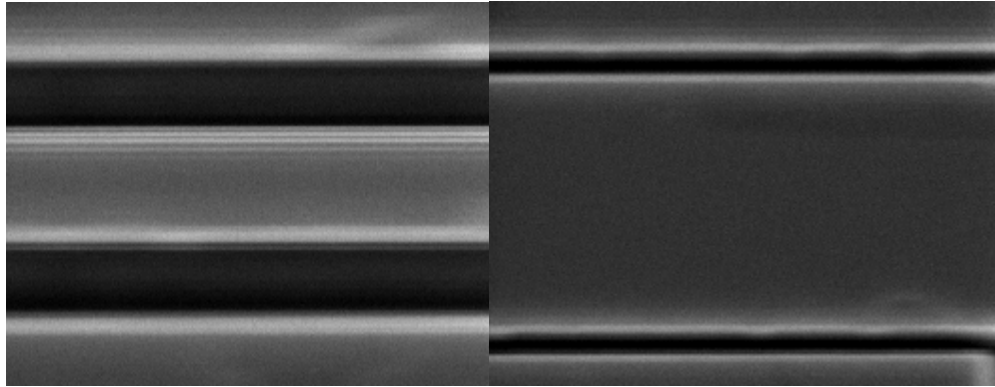


Figure 20. 7500x SEM Micrographs of 1.7 μm and 14 μm Structures

3. Second Batch Damage Considerations

In the second sample batch optical measurements near the FIB etched wire structures displayed luminous intensities over 10 times higher than measurements taken in the same regions of the first sample batch. While less damage was done to the samples, the absolute intensity in these regions was still almost 100 times lower than that of the control sample.

The 700 nm wire demonstrated both light and dark regions under SEM and CL measurements and visible variation in its width and structure. All wire structures also demonstrated surface irregularities in the regions surrounding the FIB milling. The second batch samples were exposed to multiple RTA and chemical processes and the observed data indicate that these processes could have damaged or degraded the materials. Figure 21 shows the surface irregularities in the vicinity of the 700 nm wire as well as the irregularities within it.

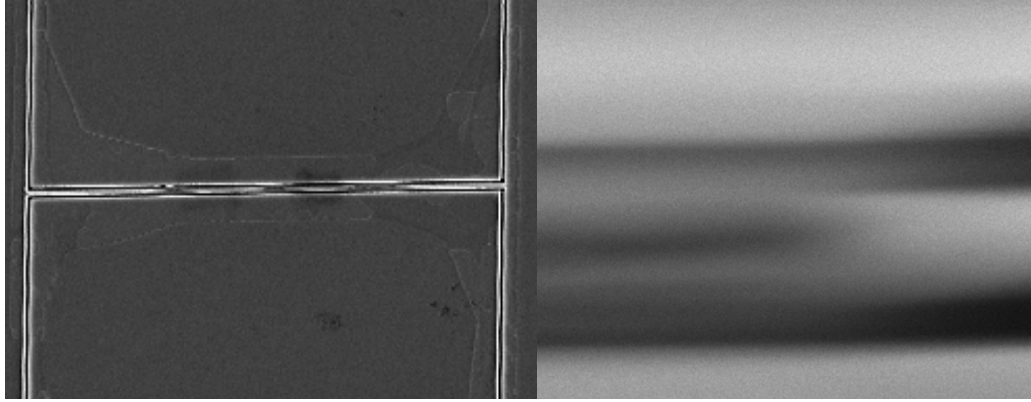


Figure 21. 550x and 12000x SEM Micrographs of 746 nm Wire
Damage

E. THIRD SAMPLE BATCH

1. Batch Fabrication Details

The third sample batch was fabricated with a focus on avoiding both overprocessing and direct exposure to the FIB etching, the presumed causes of the decreased luminescence in previous batches. A heterostructure sample was cut into five parts and in order to further test damage theories a pressed In protective cover was placed on one of the samples. All of the samples were then put in the FIB chamber.

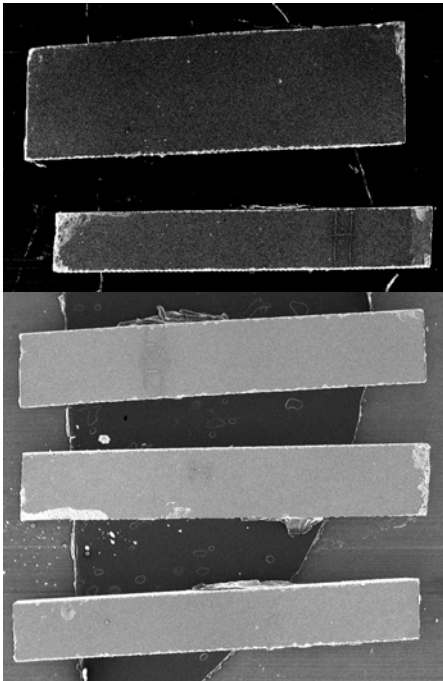
A $50\text{ }\mu\text{m} \times 100\text{ }\mu\text{m}$ area was FIB etched at 500 pA for 0.2 seconds and another $23\text{ }\mu\text{m} \times 33\text{ }\mu\text{m}$ area was FIB etched at 500 pA for 2 minutes on the In protected sample. Two $\approx 0.5\text{ }\mu\text{m}$ wire structures were also etched on this sample using both an 8 minute 500 pA FIB exposure and 40 minute 30 pA FIB exposure.

Wire structures were then FIB etched into three of the remaining four samples, with the fourth serving as a control sample. The samples were then rinsed in HCl solution for 30 seconds and pressed In contacts were added

to individual samples as required for application of external bias.

2. Batch Sample Dimensions

The third sample batch was fabricated with one larger ($\approx 6.5 \mu\text{m}$) and three smaller ($\approx 0.5 \mu\text{m}$) wire structures. A significant increase in the consistency of the wire widths was also observed over the last two batches, and one 300 nm wire was constructed. Average sample dimensions were acquired through line scans from the SEM and the degree of uncertainty in the measurements correlates directly to the intensity contrast, however, in the case of the 300 nm wire, the resolution limitations of the SEM rather than the wire quality determined the errors in measurement.



Sample Number	Wire Width (nm)	Error (nm)	Error (%)
1	6529	± 35	0.54
2	489	± 15	3.07
3	571	± 20	3.50
4	300	± 30	10.0

Table 4. Third Batch Sample Dimensions

Figure 22. 100x SEM Micrograph of Third Batch Samples

F. FOURTH SAMPLE BATCH

1. Batch Fabrication

The fourth batch of wire structures was etched with a FIB directly into the already contacted and functional sample that was used as a control in the third batch of experiments. This was done to avoid contacting difficulties present in previous samples and to have extensive pre-FIB exposure drift and intensity measurements for comparison with the fourth batch samples.

The use of box templates in the FIB patterning software allowed for a more accurate FIB pattern on the sample, eliminating the width variations occasionally produced by line template patterning used previously. The sample was etched with 10 minute, 500 pA series exposures of the FIB.

2. Batch Sample Dimensions

A series of four wires were fabricated on the fourth sample batch, ranging in width from approximately 0.8 to 9 μm . Figure 23 shows a high definition 1000x SEM micrograph of the fourth batch samples etched into the GaAs double heterostructure. The vertical dimension of the wires is $\approx 153.5 \mu\text{m}$.

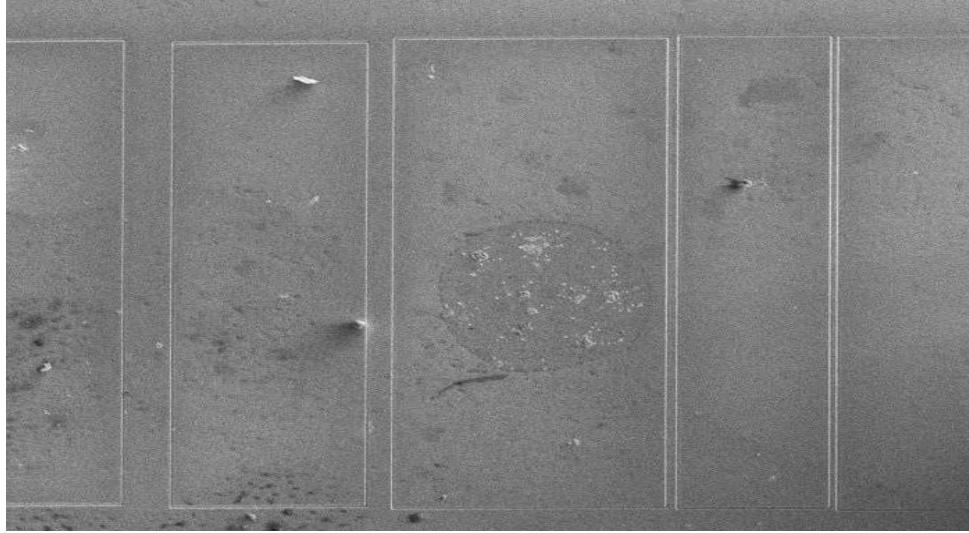


Figure 23. 1000x SEM Micrograph of Fourth Batch Sample

Average sample dimensions, shown in Table 5, were acquired through line scans from the SEM and the degree of uncertainty in the measurements correlates directly to resolution limitations of the SEM.

Sample Number	Wire Width (nm)	Error (nm)	Error (%)
1	9258	±20	0.36
2	4850	±25	0.36
3	1632	±20	1.16
4	792	±20	4.69

Table 5. Fourth Batch Sample Dimensions

IV. EXPERIMENTAL RESULTS

A. INTRODUCTION

The results of the characterization work can be broken down into two main categories, intensity and drift measurements on the top-down GaAs wire structures and the initial observation of luminescence from the bottom-up GaN and ZnO nanowire structures. The top-down wire structure results are further divided into their respective batches, while the bottom-up structures are divided into SEM and CL imaging, CL spectra and CCD imaging.

B. TOP-DOWN WIRE STRUCTURES

1. First and Second Sample Batches

The first and second batches represented initial attempts at production of samples displaying 1D confinement. As discussed in the previous chapter, significant damage was observed after FIB etching and recorded via luminescence decreases in both the first and second batch samples. This was initially attributed to the multi-step processing that the samples underwent.

Spot intensity measurements were done on the second batch samples and an overall pattern of decreasing average intensity was observed as the wire structure dimensions decreased. Average spot intensities are shown for the four different second batch sample wire structures under the same electron beam excitation of 1×10^{-10} A at 30 keV in Figure 24.

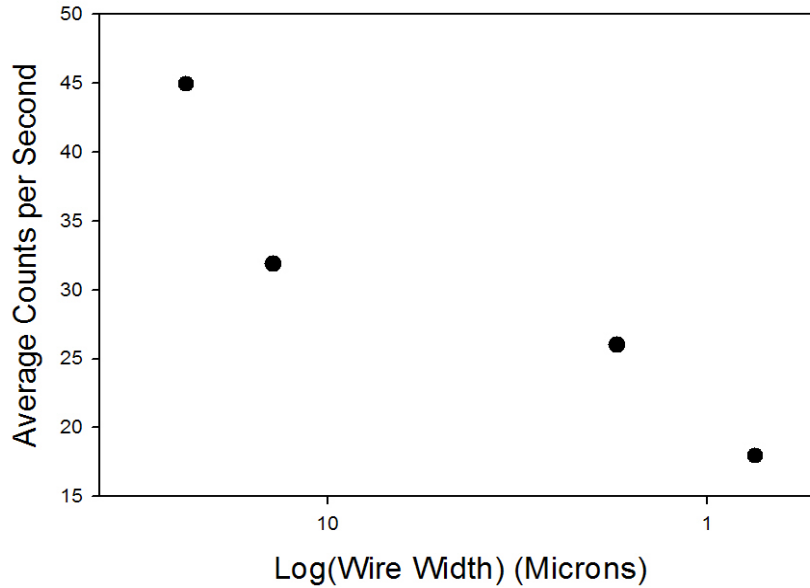


Figure 24. Comparison of Average Second Batch Wire Structure Intensity

2. Third Sample Batch

The third sample batch provided a quantitative measurement of the FIB damage to the samples, a comparison of wires etched at different FIB currents and initial contacting and drift measurements. The third batch control sample was successfully contacted and drift measurements were carried out on it, but those results are presented in the next section due to their relevance to batch four.

The third batch samples were contacted using pressed In contacts and the resistances of the contacted samples were measured using a fine tipped probe station. Resistance values were far below the control sample scaled values, as displayed in Table 6. The significantly lower than predicted resistances and the inability to observe drift in the third batch samples led to concern for the quality of electrical contacts on the samples and raised the

possibility of parallel conduction paths due to surface damage.

Sample	Control	24 μm	14 μm	1.4 μm	0.7 μm
Measured Resistance ($\text{k}\Omega$)	0.3	7	9.4	41.6	120
Predicted Resistance ($\text{k}\Omega$)	N/A	18.5	31	251	592

Table 6. Third Batch Contacted Sample Resistance

Using an In protective layer on one of the samples allowed for three regions of different FIB exposure to be tested. A 50 μm x 100 μm area was FIB etched at 500 pA for 0.2 seconds and a second 23 μm x 33 μm area was FIB etched at 500 pA for 2 minutes. The CCD image in Figure 25 shows the intensity contrast between the 0.2 and 120 second FIB exposed regions (light and dark respectively). The average intensity results on the In protected and FIB exposed regions of the sample are displayed in Table 7.

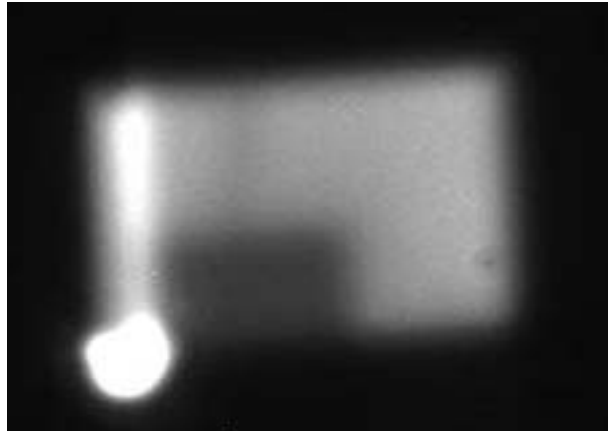


Figure 25. 2000x, 30 keV, 1×10^{-10} A, 5 Second SEM Picture Mode
CCD Exposure

Region of Interest	Average Intensity (CCD Counts)
In Protected Region	7201
0.2 Sec, 500 pA Exposure	2391
120 Sec, 500 pA Exposure	1994

Table 7. Average Maximum 0.25 Second Spot Intensities, 30 keV, 1×10^{-10} A

Third batch samples also served to examine the intensity differences of wires etched at different FIB currents. Table 8 displays the average intensity from the 489 nm 8 minute 500 pA FIB exposure and the 571 nm 40 minute 30 pA FIB exposure wire structures. This was evidence that the exposure amperage in the FIB did not change the luminescence of the wire structures significantly.

Region of Interest	Average Intensity (CCD Counts)
489 nm, 500 pA Exposure	544
571 nm, 30 pA Exposure	584

Table 8. Average Maximum 1 Second Spot Intensities, 30 keV, 1×10^{-10} A

3. Fourth Sample Batch

In order to control as many factors as possible and potentially observe carrier drift in the samples, the fourth batch of wires was etched with a FIB directly into the already contacted and functional sample that was used as a control in the third batch of experiments. Fourth batch sample wire structures displayed higher luminous intensities and greatly decreased variations in width due

to the refinement of the FIB etching process employed to fabricate them.

Extensive spot intensity measurements were done on the fourth batch samples. Consistent with the second batch observations, as the wire structure dimensions decreased, an overall pattern of decreasing average intensity was observed. The average intensity observed on the widest structure is a factor of ≈ 65 less than the initial (pre-FIB processed) material. The average spot intensities in the four fourth batch sample wire structures are shown in Figure 26.

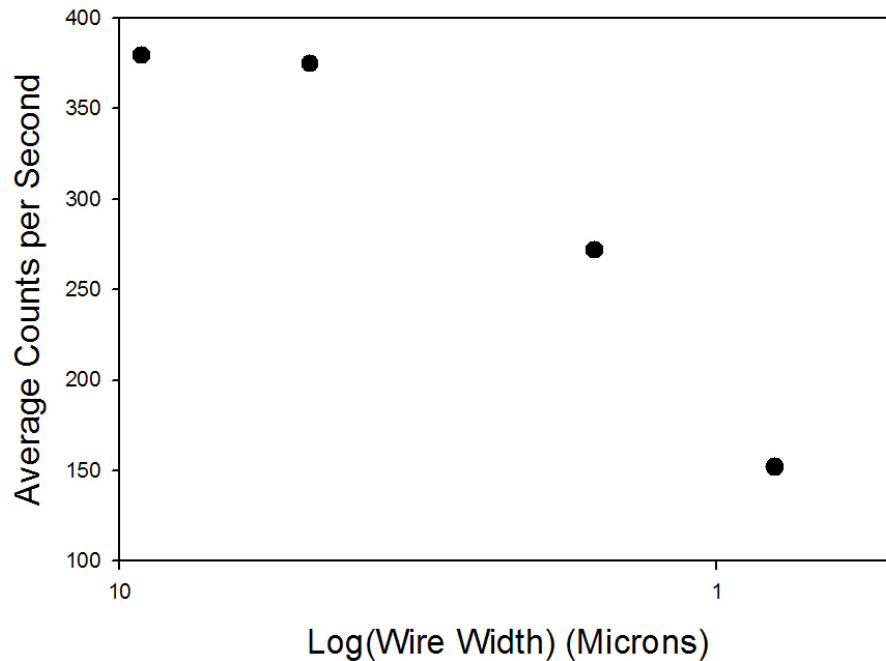


Figure 26. Comparison of Average Fourth Batch Wire Structure Intensity

In order to analyze drift in the fourth batch wire structures, it is important to first examine drift data from the contacted heterostructure used as the control sample in the third batch experiments. Figure 27 shows data

obtained from the sample before it was exposed to the FIB at fields of zero and ≈ 0.01 V/ μm and Figure 28 shows line scans of the same unexposed sample.

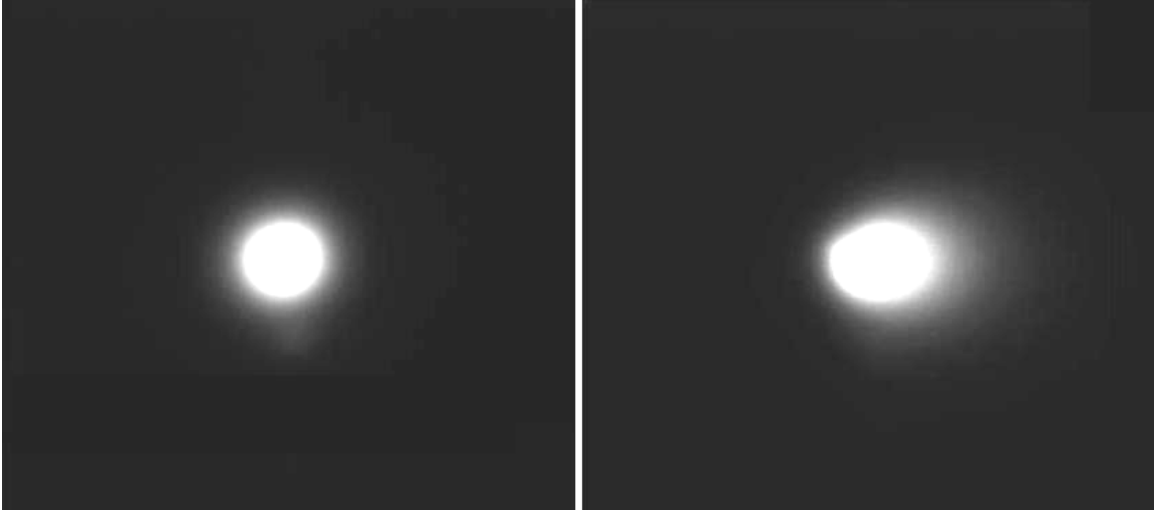


Figure 27. 30 keV, 1×10^{-10} A, 0.35 Second Spot on GaAs Heterostructure, 0 and 20V bias ($170 \mu\text{m} \times 160 \mu\text{m}$)

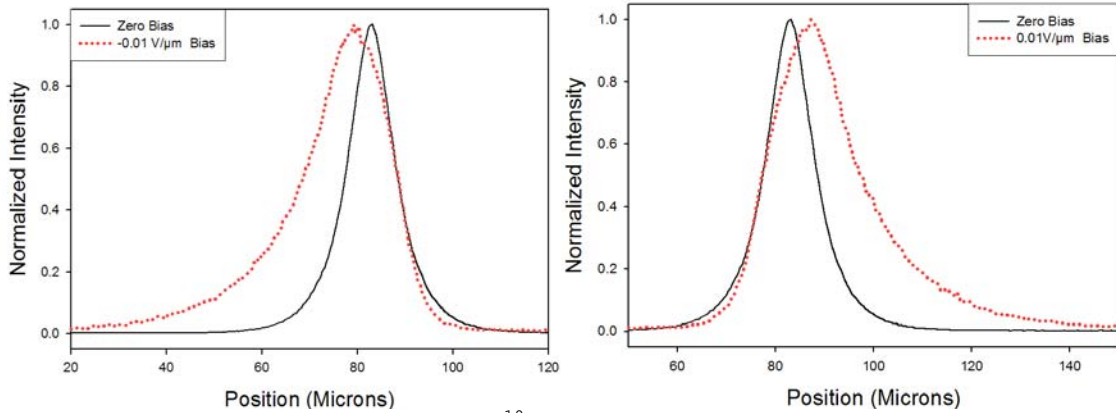


Figure 28. 30 keV, 1×10^{-10} A, 0.35 Second Spot Linescans on GaAs Heterostructure, 0 and ± 0.01 V/ μm bias

Using the same contacts, potential differences of up to 20 volts were applied to the sample after the FIB etching of wire structures. A sample resistance of 908Ω was measured and there was optical evidence of an applied field. Changes in spot intensity from 152 counts per second at no bias to 33 counts per second at 20V bias also serve

as a clear indication that field was applied to the sample. Assuming that the voltage dropped at the contacts remained similar, an approximate potential difference of ≈ 0.13 V/ μm was applied during experiments. Figure 29 shows two CCD images taken at different bias on the smallest (≈ 0.8 μm) wire structure and Figure 30 shows line scans across the same data. These results are further discussed and analyzed in Chapter V.

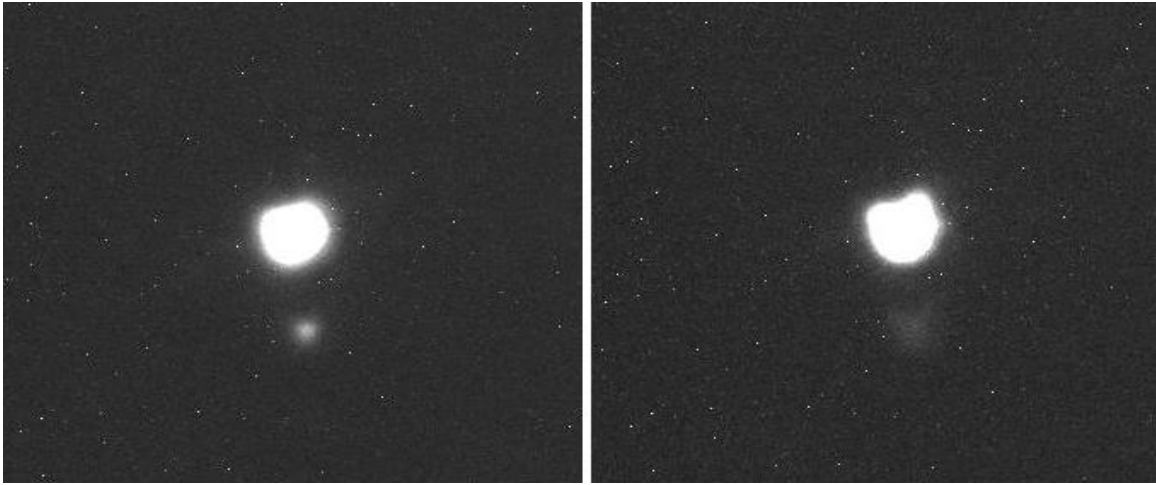


Figure 29. 30 keV, 1×10^{-10} A, 20 Second Spot on 0.8 μm wire structure, 0 and 20V bias (136 μm x 117 μm)

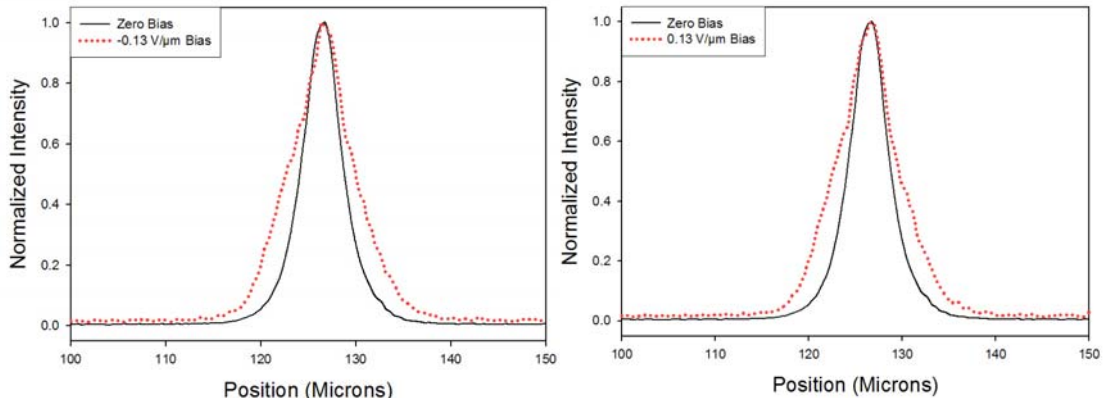


Figure 30. 30 keV, 1×10^{-10} A, 20 Second Spot Linescans on 0.8 μm wire structure, 0 and ± 0.13 V/ μm bias

C. BOTTOM-UP WIRE STRUCTURES

1. SEM and CL Micrographs

The first step in expanding the transport imaging technique to nanowires involved locating the nanowires on their respective substrates and recording SEM and CL micrographs to determine the spectra and magnitude of luminous emission. It is important to note that the CL system collects all light emitted from any point in the image and maps it to the point on the image that is being exposed to the electron beam, so it is used to provide a general idea of the panchromatic intensity of the sample or the intensity of the sample at a selected wavelength, but its spatial information assumes that charge generation and luminescence arise from the same point.

ZnO and GaN nanowires were deposited on Gold and SiO₂ substrates but could only be located on the SiO₂ substrate, possibly due to chemical interaction and decomposition of the nanowires with the Au substrate. ZnO and GaN nanowires and nanowire groups were observed to be bright on SEM micrographs mainly due to charging because of their electrical isolation on the SiO₂ substrate. Figures 31 and 32 show SEM micrographs of ZnO and GaN nanowire groups at 2000x and isolated nanowires at a magnification of 4000x on the SiO₂ substrate. The measured diameters of 10-200 nm and aspect ratios of 10-100 of the nanowires were consistent with expected values [17,18,19] for both GaN and ZnO.

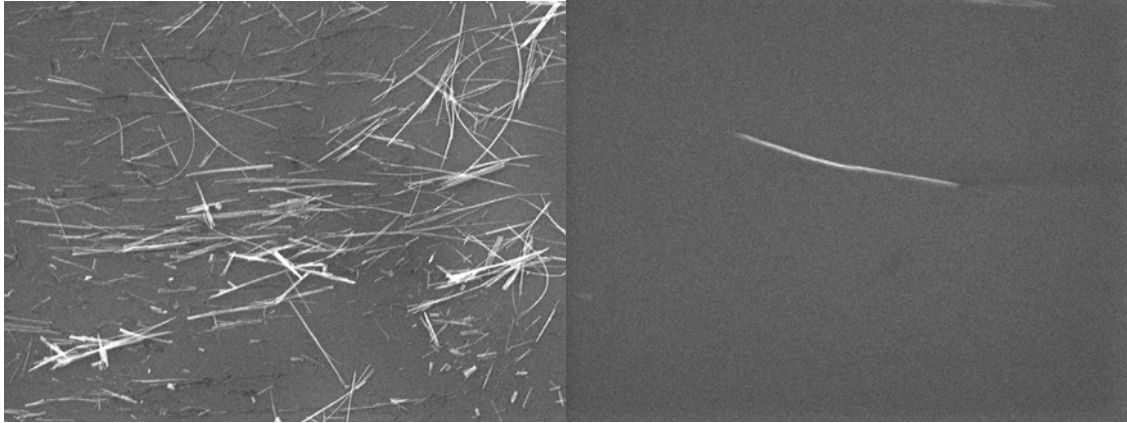


Figure 31. 2000x and 4000x SEM Micrographs of ZnO Nanowires, 15 keV, 1×10^{-10} A

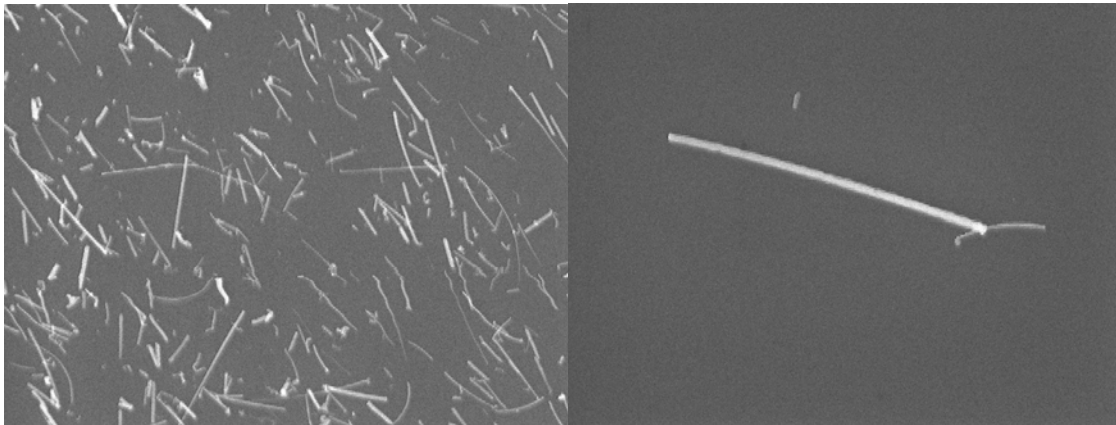


Figure 32. 2000x and 4000x SEM Micrographs of GaN Nanowires, 15 keV, 1×10^{-10} A

After the initial SEM micrographs were taken, the CL system was activated in parallel with the SEM, allowing for simultaneous SEM and CL imaging. The CL system was set to panchromatic mode in order to achieve maximum intensity for the micrographs. The results for the ZnO nanowires are displayed in Figure 33.

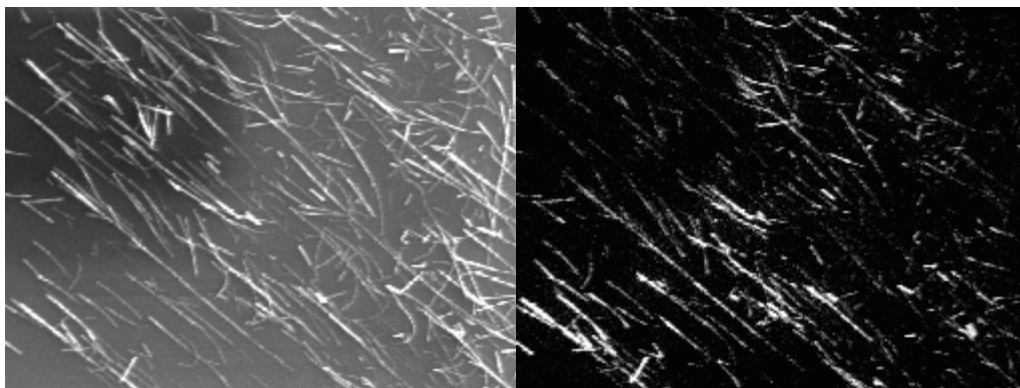


Figure 33. 2000x SEM (left) and CL (right) Micrographs of ZnO Nanowires, 15 keV, 1×10^{-10} A

CL images were also taken at 2000x on the GaN nanowires in panchromatic mode, as shown in Figure 34. The panchromatic CL image was nearly featureless in the GaN case at magnifications of 2000x due to strong substrate emissions in the background; however some individually luminescent wires were visible.

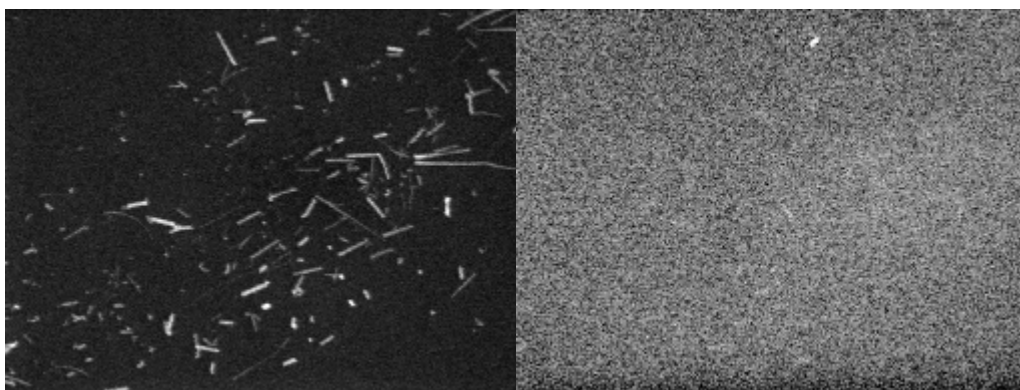


Figure 34. 2000x SEM (left) and CL (right) Micrographs of GaN Nanowires, 15 keV, 1×10^{-10} A

Further examination of the strongly luminescent regions on the GaN nanowire sample at higher magnification led to successful CL imaging on that sample. Individual GaN nanowires are visible in the 10000x CL image in Figure 35.

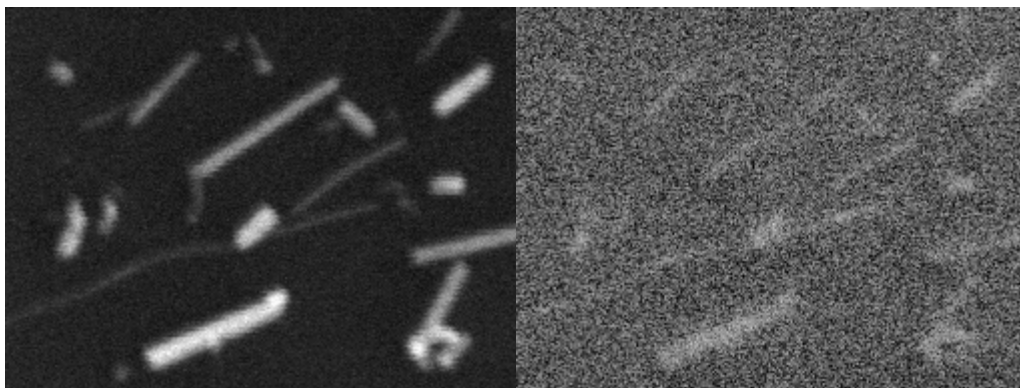


Figure 35. 10000x SEM (left) and CL (right) Micrographs of GaN Nanowires, 15 keV, 1×10^{-10} A

2. Cathodoluminescence Spectra

CL spectra were taken on the ZnO and GaN nanowire and substrate regions in order to determine the wavelength distribution of the panchromatic data taken in the CL micrographs. CL spectra were taken between 300 nm and 700 nm with steps of 1 nm, to identify characteristic nanowire emission and distinguish it from the substrate emission.

ZnO nanowires displayed a very strong peak at about 378 nm (3.29 eV), visible in Figure 36.

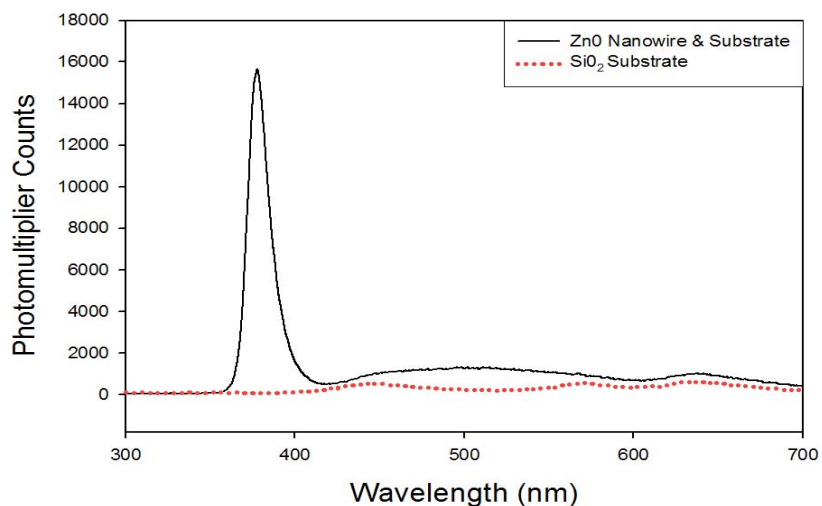


Figure 36. CL Spectra of ZnO Nanowires and SiO₂ substrate, 15 keV, 1×10^{-10} A

The GaN nanowire spectra had to be directly compared to substrate spectra in order to clearly indentify an emission peak. In Figure 37, a small deviation from the substrate spectra can be seen in the GaN nanowire spectra in the vicinity of 350-450 nm and corresponds to a peak at about 380 nm (3.27 eV).

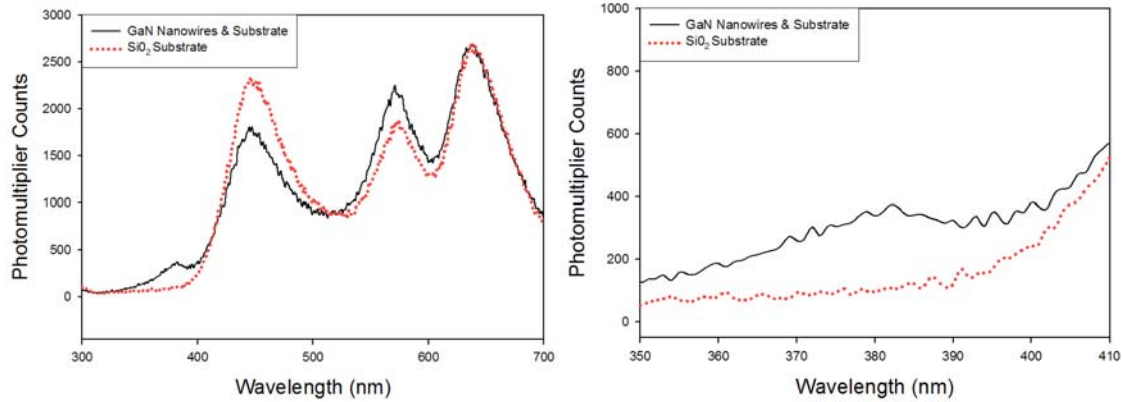


Figure 37. CL Spectra of GaN Nanowires and SiO₂ substrate, 15 keV, 1×10^{-10} A

The observed spectral peaks associated with the nanowires are in agreement with expected values of ZnO and GaN bandgaps of ≈ 3.3 eV and ≈ 3.4 eV respectively at 300K [16,17].

3. CCD Imaging of Nanowires

The data gathered during CL clearly indicate that the nanowires luminesce; however, the CL system employs a high voltage photomultiplier while the CCD system records directly emitted intensity without any optical amplification. In order for the transport imaging technique to be employed on nanowires they must be visible on the CCD system.

The final results taken on the nanowire samples were a series of unfiltered CCD images in which GaN and ZnO nanowires' spatial luminescence was resolved with the OM and CCD system used for transport imaging. In Figure 38 a group of GaN nanowires are imaged with the CCD, in Figure 39 two single ZnO nanowires are imaged.

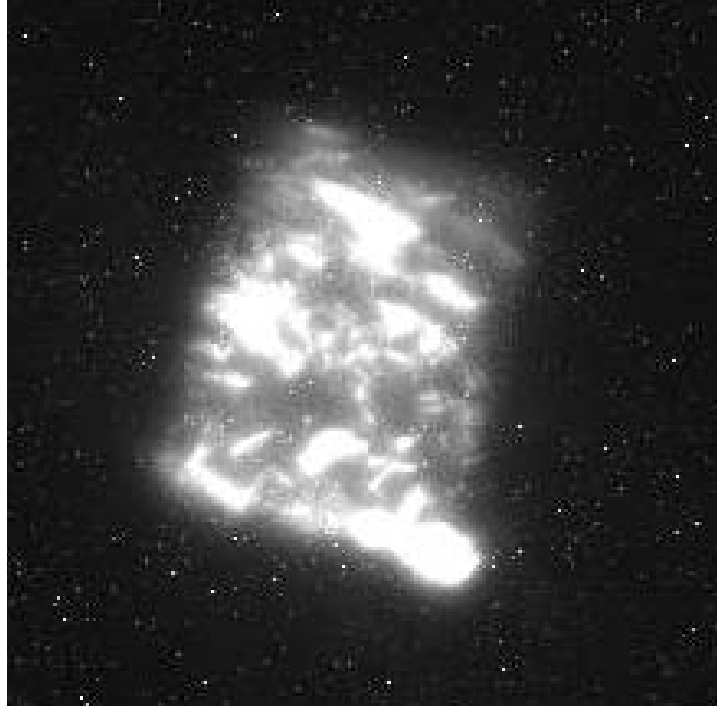


Figure 38. 2500x, 15 keV, 1×10^{-10} A, 120 Second Image of GaN Nanowires



Figure 39. 2000x, 30 keV, 1×10^{-10} A, 120 Second Image of ZnO Nanowires

V. CONCLUSIONS AND SUGGESTIONS FOR FURTHER RESEARCH

A. SUMMARY AND CONCLUSIONS

1. Top-Down Wire Structures

Throughout the research on top-down wire structures four separate sample batches were fabricated and various intensity and drift measurements were made on the samples. Extensive experience with the FIB system and samples allowed for a progressive refinement of the FIB etching process employed to fabricate the structures, however, there was a significant decrease in average luminous intensity in all samples that were exposed to the FIB. Many wire structures displayed evidence of electrical contacting problems and even those which were contacted effectively did not display measurable drift.

Initial FIB etching resulted in average decreases in luminous intensity of over a factor of 1000 from the unexposed AlGaAs/GaAs/AlGaAs double heterostructure and wire structures of poorly defined edges and widths. Reduction in the processing of the sample and experience with the FIB system and the patterning software yielded significant increases in the wire structures' quality and reduced the average decreases in luminous intensity to a factor of 65.

Although the latter sample batches' loss of intensity and structural variation was significantly lower than earlier batches, all the top-down wire structure batches demonstrated a consistent pattern: Figure 40 shows that in

all measured samples, as the wire structure dimensions decreased so did the average intensity.

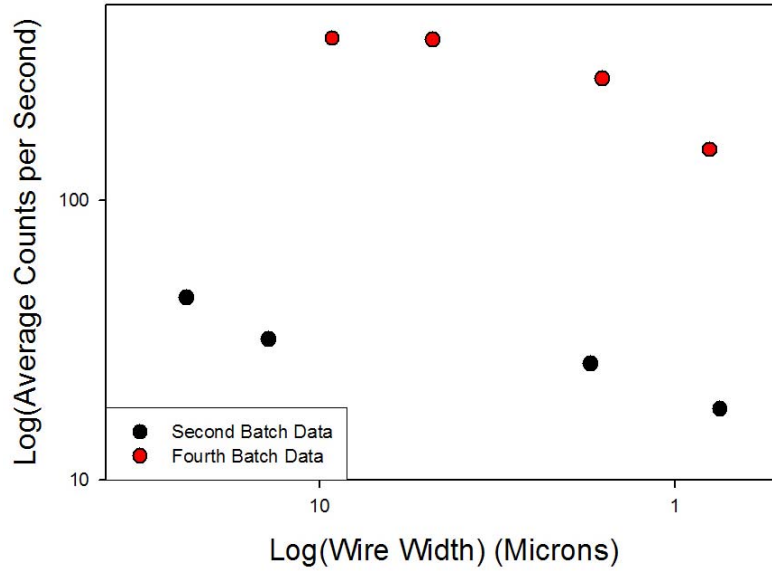


Figure 40. Comparison of Average Second and Fourth Batch Wire Structure Intensities

Changes in electrical properties of samples due to FIB exposure have been recorded in the past and characterized as ion-induced surface defects and passivation of dopants due to surface amorphization [20,21]. Ion induced surface defects could serve as extra scattering centers in the vicinity of the FIB etching which could change the non-radiative lifetime of the carriers within the material and subsequently, to first order, the overall lifetime and luminous intensity observed. This can be modeled as an effective decrease in diffusion length, following:

$$L_d = \sqrt{\frac{kT}{e}} \mu \tau \quad (18)$$

$$\frac{1}{\tau} = \frac{1}{\tau_r} + \frac{1}{\tau_{nr}} \quad (19)$$

where μ is the mobility, τ is the lifetime, τ_r is the radiative lifetime and τ_{nr} is the non-radiative lifetime

associated with an increase in scattering centers and point defects in the material.

Examination of the fourth top-down wire structure batch allowed a direct comparison between previously undamaged material which displayed drift and the same material after the FIB process. The unexposed sample displayed, on average $\approx 26,000$ counts per second on the CCD, while the same regions after indirect exposure to the FIB had intensities averaging ≈ 400 counts per second, a factor of 65 decrease in intensity.

Employing Equations (18) and (19) a new L_d of $0.44 \mu\text{m}$ can be calculated under the assumption that to first order, changes in intensity can be interpreted as changes in lifetime. Figure 41 shows a drift model using these modified parameters compared with the experimental results for smallest ($\approx 0.8 \mu\text{m}$) fourth batch wire structure.

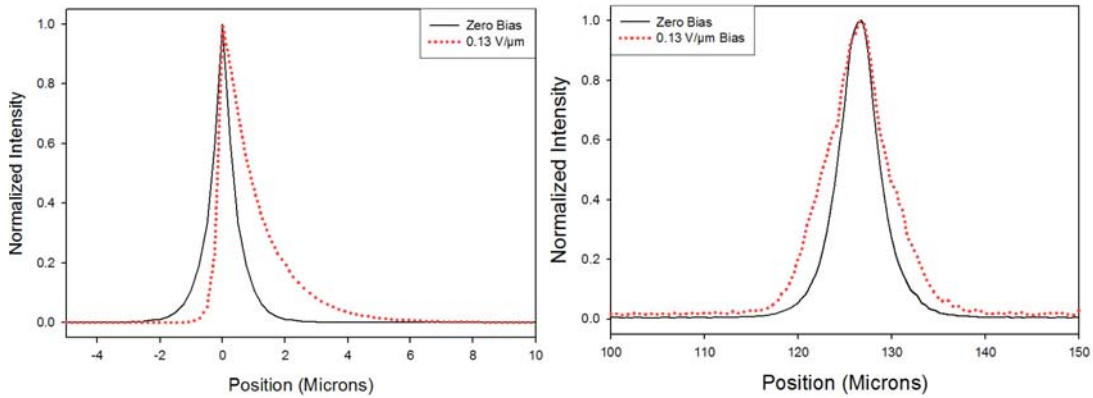


Figure 41. 0 and $0.13 \text{ V}/\mu\text{m}$ bias $L_d=0.44 \mu\text{m}$, $n=30$ Simulation (left) and 30 keV , $1 \times 10^{-10} \text{ A}$, $20 \text{ Second Spot Linescan}$

While there was a clear broadening of the normalized spot under applied bias in both directions, there was no reliable evidence of directional drift as illustrated in the modeling. The main limitation to drift measurements on

this scale is the lack of optical resolution on the CCD system, as even modeled data displayed directional drift $\geq 1.5 \mu\text{m}$, less than 4 pixels on the CCD image.

The change in effective drift length due to a change in lifetime of the minority carriers produces a model which predicts drift below the resolution of our optical system, which is consistent with the observed data. This hypothesis also effectively predicts the observed trend of decreasing intensity with decreasing wire dimensions because if a constant area around the FIB etched areas is damaged then the smaller wire structures would display a decreased luminous intensity as a larger fraction of their area would have been damaged.

Although the methods of FIB etching sample fabrication improved dramatically throughout the course of research and the loss of average luminous intensity in the samples was significantly reduced, we can conclude that, on the current apparatus, until further work has been done to characterize FIB damage, FIB etched top-down fabrication on GaAs double heterostructure material is not a viable method of imaging 1D confinement and employing the transport imaging technique. Throughout the sample testing, reduction in the average luminous intensity and the correlated reduction in diffusion length yielded changes below the optical resolution thresholds for our experimental apparatus.

2. Bottom-Up Wire Structures

ZnO and GaN nanowires on SiO_2 substrates were identified and imaged using the SEM, panchromatic CL and the CCD camera. Nanowire luminescence was also

characterized by taking CL spectra of the nanowires and the SiO₂ substrate. ZnO and GaN nanowires on Au substrates were not observable.

Both the GaN and the ZnO wires showed spectral maxima that occurred in the vicinity of 380 nm, at a higher energy than most of the broadband spectra of the SiO₂ substrate. Short wavepass filters could easily be employed to reduce the amount of background light in the system during measurements and further decrease the substrate intensity (noise) in CCD pictures in future experiments.

Further research into the Au substrates' chemical interaction with the GaN and ZnO nanowires to determine the causes of nanowire disintegration or lack of luminescence could also be pursued, however this is less critical because future wire structures will be on SiO₂ substrates. We can conclude that luminescence of the quantum wires can be imaged and that their emission spectra are consistent with expected values. This data serves as a strong indication of the feasibility of expanding the transport imaging process to 1D bottom-up nanowires.

B. SUGGESTIONS FOR FURTHER RESEARCH

1. Advances in Bottom-Up Nanowire Structures

The fabrication of contacted nanowires is the next step in the application of the transport imaging method to 1D nanowires. Currently nanowires are grown on the substrate surface by CVD and remain uncontacted. Research groups fabricating single nanowire devices have reported the ability to move individual nanowires and contact them [4,18,19].

Contacted nanowires would allow for initial qualitative observation of drift in 1D structures, and coupled with increased system optical resolution could yield the first quantitative drift measurements. High resolution drift measurements could then be used to extract transport parameters directly from CCD images of the nanowires.

2. Increased System Resolution for Transport Imaging

In this work, the use of an optical microscope, internal to an SEM, to directly image the spatial recombination of charge generated by electron irradiation in nanowires has been demonstrated. However, the current system resolution is ≈ 400 nm/pixel and even in these preliminary examinations of nanowire structures, the apparatus has been pushed near the limits of its optical resolution.

A new National Science Foundation grant has been obtained to advance the technique to higher resolution using near field optical techniques. A near field microscope, with special open architecture for use inside a SEM, could increase resolutions of ≈ 50 -100 nm, and has been ordered from Nanonics Inc. and should be installed by summer 2006.

Increased system resolution would be a very important step towards quantitative transport imaging measurements in nanowire structures as well as in materials which display very short diffusion lengths such as GaN. System resolutions of 50-100 nm would also allow for empirical verification of the reduced diffusion length hypothesis in

FIB etched top-down structures and for imaging of 1D confinement in bottom-up nanowire structures.

3. Transport Imaging as a Measurement of FIB Damage

Most analyses of FIB damage use MonteCarlo simulations models and analysis of damage layer thickness and damage processes by TEM [20]. TEM studies have also shown that the damage layers are amorphized by the FIB, but results gathered from the top-down wire structures indicate that FIB etching may produce electrical damage that is more extensive than structural damage visible by TEM.

An in depth exploration of FIB damage by means of transport imaging could provide a very sensitive measurement of sample damage at an electronic or point defect scale. Quantitative studies would have to be undertaken in different materials and different FIB exposure times and energies.

More research and experimentation would also have to be done to determine if the observed decreases in luminous intensity do in fact correspond to decreases in lifetime within the material. Confirmation of the hypotheses presented in this paper could involve independent Time Resolved Photoluminescence (TRPL), in which the sample is excited by a picosecond pulsed laser and radiative carrier lifetime can be accurately measured.

THIS PAGE INTENTIONALLY LEFT BLANK

APPENDIX A: DATA EXTRACTION PROGRAM

```
1      %Data.m Made by stephen winchell
2      %Last Modified, Feb 3, 2006
3      %Function to extract the Row and Col Max from CCD Image
4      %Maxima marked by cross for visual error-check
5      %Median noise filtering and noise subtraction from max value
6
7      function [colmax, rowmax]=data(pic);
8
9      %input image file to matlab and convert it to double to work with
      later
10     I = imread(pic);
11     I = double(I);
12     imagesc(I)
13
14     %do a median noise filtering on the image
15     J = medfilt2(I);
16     imagesc(J)
17
18     %take off the noise floor by subtracting the average of the
      smallest sum of a row or col
19
20     [rows, cols] = size(J);
21     colsum = sum(J);
22     rowsum = sum(J');
23
24     if (min(colsum)/cols) <= (min(rowsum)/rows)
25         noisefloor = min(colsum)/cols;
26     else
27         noisefloor = min(rowsum)/rows;
28     end
29
30     %find the maxima and plot it
31     maxcols = max(J);
32     maxrows = max(J');
33     [colmax, xposition] = max(maxcols);
```

```
34     [rowmax, yposition] = max(maxrows);
35     colmax = colmax - noisefloor
36     rowmax = rowmax - noisefloor
37
38     hold;
39     plot(xposition, yposition, 'c+')
```


LIST OF REFERENCES

1. Lieber C. M., *Sci. Am.*, September (2001).
2. Alferov Z. I., *Semiconductors* **32**, 1 (1998).
3. Huang Y., Duan X., Lauhon L. J., *Science* **294**, 5545 (2001).
4. Duan, X., Agarwal, R., Lieber C. M., *Nature* **421**, 6920 (2003).
5. Huang M. H., Mao, S., Feick, H., *Science* **292**, 5523 (2001).
6. Haegel N. M., Fabbri J. D., Coleman M. P., *Appl. Phys. Lett.* **84**, 8 (2004).
7. Lubner D. R., Bradley F. M., Haegel N. M., Talmadge M., Coleman M.P., *Appl. Phys. Lett.* in review 2006.
8. Yacobi B. G., Holt D. B., *Cathodoluminescence Microscopy of Inorganic Solids*. (Plenum, New York, 1990)
9. Weisstein E. W., *MathWorld*, A Wolfram Web Resource.
<http://mathworld.wolfram.com/FullWidthatHalfMaximum.html>,
Last Access: June 2006
10. Klein, C. A., *J. Appl. Phys.* **39**, 2029 (1968).
11. Kayana, K., Okayama, S., *J. Appl. Phys.* **5**, 43 (1972).
12. Bracewell, R., *The Fourier Transform and Its Applications*, 3rd ed. (McGraw-Hill, New York, 1999)
13. Arfken, G. B., Weber, H. J., *Mathematical Methods for Physicists*. (Academic Press, San Diego, CA, 2001)
14. Lee, S. K., Choi H. J., Pauzauskie, P., Yang P. D., Cho, N. K., Park H. D., Suh E. K., Lim K. Y., Lee, H. J., *Physica Status Solidi B* **242**, 3 (2005).
15. Sutton D., Parle S. M., Newcomb S. B., *Electron Microscopy and Analysis 2001 Institute of Physics Conference Series*, **168** (2001).

16. Shan W., Schmidt T. J., Yang X. H., Hwang S. J., Song J. J., Goldenberg B., *Appl. Phys. Lett.* **66**, 985 (1995).
17. Yang, P. D., *Proceedings of the SPIE* **5349**, 1 (2004).
18. Kim J., Oh H., So H. M., *Nanotechnology* **13**, 5 (2002).
19. Law M., Goldberger J., Yang P.D., *Annual Review of Materials Research* **34** (2004).
20. Xia, L., Wu W., Wang Y., *Appl. Phys. Lett.* **88**, 152108 (2006).
21. Boxleitner, W., Hobler, G., Klüppel, V., Cerva, H., *Nuclear Instruments and Methods in Physics Research*, **175-177** (2001).

INITIAL DISTRIBUTION LIST

1. Defense Technical Information Center
Ft. Belvoir, Virginia
2. Dudley Knox Library
Naval Postgraduate School
Monterey, California
3. Professor Nancy M. Haegel
Naval Postgraduate School
Monterey, CA
4. Professor James Luscombe
Naval Postgraduate School
Monterey, CA
5. Thomas Boone
Hitachi Global Storage
San Jose, CA
6. Dave Luber
Headquarters United States Marine Corps
Washington, DC